International Forum on Aeroelasticity and Structural Dynamics
IFASD 2024
17-21 June 2024, The Hague, The Netherlands

UNSTEADY RANS-BASED COMPUTATIONAL AEROELASTIC SIMULATIONS OF X-56A FLUTTER FOR THE THIRD AEROELASTIC PREDICTION WORKSHOP

Iren A. Mkhoyan[1,2], **Peter H. L. Blom**[1], **Jos V. J. E. Aalbers**[1], and **Huub S. Timmermans**[1]

[1]Royal Netherlands Aerospace Centre
Anthony Fokkerweg 2, 1059CM Amsterdam, The Netherlands
Iren.Mkhoyan@nlr.nl
Peter.Blom@nlr.nl
Jos.Aalbers@nlr.nl
Huub.Timmermans@nlr.nl

[2]Delft University of Technology
Kluyverweg 1, 2629HS Delft, The Netherlands
A.Mkhoyan@tudelft.nl

Keywords: Computational aeroelasticity, RANS, structural dynamics, modal analysis, body freedom flutter, generalised aerodynamic forces

Abstract: This paper presents a high-fidelity aeroelastic study of the the Multi-Utility Technology Testbed (MUTT) X-56A, designed to exhibit aeroelastic instabilities such as body free flutter (BFF). The primary objective of this work is to assess the use of high-fidelity CFD-based aeroelastic simulations for flutter prediction. This research was originally conducted as part of the Third Aeroelastic Prediction Workshop (AePW3) aiming to enhance the knowledge in aeroelastic predictions using mid to high-fidelity computational aerodynamics. This particular study details the contribution from the Flight Physics Loads group at the Netherlands Aerospace Centre (NLR), exploring two computation methods for generating the Generalised Aerodynamic Forces (GAFs), namely, ZAERO solver (ZONA Technology) using higher-order panel code ZONA6, and an unsteady RANS-based Computational Fluid Dynamics (CFD) and Computational AeroElastic (CAE) simulations implemented within NLR's ENFLOW simulation system for multi-block flow domains. The high-fidelity CFD and CAE analyses were performed using the flow solver ENSOLV with unsteady Reynolds-Averaged Navier-Stokes (RANS) flow formulation implemented with Explicit Algebraic Reynolds Stress Model (EARSM) turbulence modelling based on the TNT $k-\omega$. The CAE computational procedure consists of four tool chains, involving structural dynamics (modal) analyses; grid interpolation procedure; steady CFD computations on the undeformed shape; unsteady CFD computations on a deforming grid under prescribed, small-amplitude sinusoidal excitations based on the structural mode shapes; and the transformation of the time-domain unsteady solutions to frequency domain in order to construct the GAF matrices. The X-56A configuration used for this study is the 10lb fuel state model released within the AePW-3 group. The resulting GAFs were compared to the ZAERO results, showing good agreement for both the rigid body and elastic modes. Earlier work on X-56A within AePW-3 conveyed the need for further refinement of the high-fidelity aeroelastic methodology. Improvement efforts in this regard, included alternative structural dynamics methods for modal model computations, CFD grid refinements, and adjustments to the (un)steady CFD/CAE simulation procedures and methods.

Figure 1: X-56A Multi-Utility Technology Testbed (MUTT) in flight demonstration [credit: NASA/Jim Ross [1]]

1 INTRODUCTION

The third Aeroelastic Prediction Workshop (AePW-3) series is intended to provide an open forum, to encourage transparent discussion of results and processes, to promote best practices and collaborations, and to develop analysis guidelines and lessons learned. Within the AePW-3 there are four focus areas of interest: transonic flutter including shock buffet, hypersonic aeroelasticity, geometrically nonlinear wing deflections at low speed, and prediction and control of BFF. Accordingly, the AePW-3 efforts were distributed along four working groups, of which the Flight Test Working Group (FTWG) was dedicated to research, development of knowledge and expertise, and dissemination of practices and results related to aeroelastic flutter predictions and active flutter control technologies. The X-56A Multi-Utility Technology Testbed (MUTT), depicted in Fig.1, was chosen as the test case for these studies.

The X-56A MUTT is a subscale, modular, unmanned experimental air vehicle developed by Lockheed Martin Skunk Works® (Lockheed Martin Corporation, Bethesda, Maryland) under the Multi-Utility Aeroelastic Demonstrator (MAD) programme, sponsored by the Air Force Research Laboratory (AFRL) [2, 3]. Under its Body Freedom Flutter (BFF) research program, Skunk Works® sought to demonstrate the effectiveness of active control technology for flutter suppression and gust load alleviation on the X-56A, which was explicitly designed to exhibit three flutter phenomena within its flight envelope characterised by the coupling of (low frequency) flexible structural modes with the aircraft's rigid body motion. The first dynamic instability exhibited by this model is the Body Freedom Flutter (BFF) phenomenon which onsets due to the coupling between the rigid body short period flight dynamic mode and the first flexible wing bending mode. The other to instabilities are the symmetric wing bending-torsion (SWBT) flutter, and the anti-symmetric wing bending-torsion (AWBT) flutter. More on these dynamic instabilities in X-56A can be found in [1, 4].

After the initial flight tests commissioned by AFRL, the X-56A MUTT was transferred to National Aeronautics and Space Administration's (NASA) Armstrong Flight Research Center (AFRC) [5] for further research into advanced control technologies and lightweight structures under NASA's Advanced Air Transport Technology programme [6, 7]. The X-56A flight tests

served the purpose of inducing flutter, thereby demonstrating the onboard instrumentation's capability for accurate flutter onset prediction and the control system's effectiveness in actively suppressing aeroelastic instabilities. The research goals for the X-56 MUTT include advancing flutter-suppression technologies and enhancing the effectiveness of gust load alleviation, reducing structural weight to increase fuel efficiency and range, and increasing the aspect ratio to achieve aerodynamic drag reduction.

A similar study within AePW-3 has been performed by NASA Langley Research Center in [1]. A summary of the AePW-3 results was presented in [4]. This work details the most recent contributions from the Flight Physics Loads group at the NLR related to CFD-based aeroelastic predictions. This study also addresses improvements in prior analyses presented in [8].

2 BACKGROUND

This section first presents the configuration of the X-56A MUTT model used in this study, followed by the description of the mathematical structural dynamics, aerodynamics and aeroelastic models assumed in this study.

2.1 X-56A Aircraft Geometry

The X-56A Multi-Utility Technology Testbed (MUTT) is a subscale unmanned experimental air vehicle developed for the research of the dynamic aeroelastic phenomenon of Body Freedom Flutter (BFF) and the maturation of active control technologies for flutter suppression and gust load alleviation.To accommodate these research objectives, the X-56A MUTT was developed as a modular aircraft, equipped with four sets of easily re-configurable wings of varying degrees of flexibility. The X-56A configuration is a flying wing setup consisting of a rigid centre body and high aspect ratio flexible wings with in total ten trailing-edge control surfaces. These control surfaces encompass two trailing-edge body flaps on each side of the centre body and four wing flaps (elevons) along the trailing-edge of each wing. A schematic representation of the X-56A configuration geometry is given in Fig. 2.

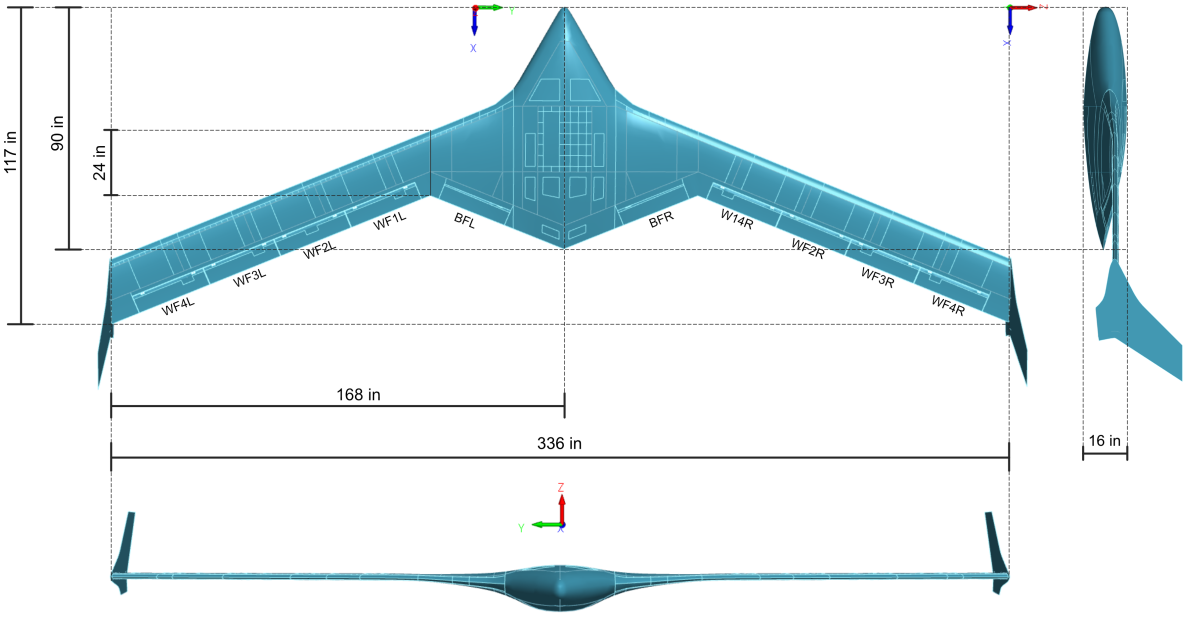

Figure 2: The X-56A geometry used in this study.

The model is designed with two P-400 JetCat turbojet engines, a non-retractable tricycle landing gear configuration and a nose boom for air data measurement [3,6,9]. These features have been omitted in the schematic above as those were not included in the CFD analyses performed in this study.

The AePW-3 investigated four different fuel states of the X-56A and its effect on the aeroelastic behaviour. However, the present study considers the lowest fuel case (i.e. 10 lb at 12.5 $\%$ of full fuel state). The aircraft configuration is equal for all cases. The dimensions, parameters and specifications of the X-56A configuration used in this study are summarised in Table 1.

Table 1: X-56A specifications, dimensions and parameters

Parameter	Symbol	Value	Units
MTOW (80lb fuel state)	W	489.1	lb
Gross Weight @ 10lb fuel state	$W_{@10\text{lb}}$	419.1	lb
Span	b	336	in
Semi-span	$b/2$	168	in
Chord Length	c	24	in
Wing Planform Area	S	8064	in^2
Aspect Ratio	AR	14	-
Wing Tip Thickness	t_{tip}	2.4	in
Wing Root Thickness	t_{root}	2.5	in
Wing Sweep Angle	Λ_{sweep}	22	deg
Moment Centre	$[x_{c_M},\ y_{c_M},\ z_{c_M}]$	$[163.5,\ 0.0,\ 104.0]$	in
Moment Arms	$[L_{M_x},\ L_{M_y},\ L_{M_z}]$	[b, c, b]	in

The design and development of the demonstrator has been addressed in detail in [9, 10].

2.2 Structural Dynamics

The dynamic behaviour of a structure excited by an external force can be modelled as a forced multiple-degrees-of-freedom (MDOF) mass-spring-damper system where the entire structure is discretised into concentrated masses connected by a series of springs and dashpots. The corresponding mathematical model is obtained by balancing the external forces with the system's inertia, elastic restoring forces and dissipation mechanism. The resulting equation of motion (EOM) for a general MDOF dynamical system is:

$$\mathbf{M}_s\ddot{\mathbf{x}}(t) + \mathbf{C}_s\dot{\mathbf{x}}(t) + \mathbf{K}_s\mathbf{x}(t) = \mathbf{F}(t) \tag{1}$$

where $\mathbf{x}(t)$ is the time-dependent vector of generalised coordinates representing the state of the system at time t; the state vector includes translational and linearised rotational displacements together forming the N degrees-of-freedom (DoFs) of the system. The vectors $\dot{\mathbf{x}}\,(t)$ and $\ddot{\mathbf{x}}\,(t)$ are the generalised velocities and accelerations. The system matrices $\mathbf{M}_s$, $\mathbf{C}_s$ and $\mathbf{K}_s \in \mathbb{R}^{N\times N}$ are, respectively, the generalised structural mass, viscous damping and elastic stiffness matrices. The mass and stiffness matrices are real, symmetric and positive definite, though the latter may be positive semi-definite if the system is unrestrained [11] [12]. $\mathbf{F}(t)$ is the generalised forcing vector, where each component is a function of t associated with the corresponding generalised coordinate. Reflected in the fact that the system's coordinates are connected and their motion is respective, the system matrices are generally non-diagonal, and the EOM in Eq. 1 is therefore a coupled system of equations.

The solution strategy in modal analysis is to seek a similarity transformation such that the system can be decoupled into an equivalent system of N independent single-degree-of-freedom (SDOF) equations, while retaining the dynamic properties of the original system. Since dynamic behaviour is governed by inherent system properties independent of the input, the problem of decoupling the EOM is directly related to solving homogeneous problem, where $\mathbf{F}(t) = \mathbf{0}$ and the initial conditions are zero as well. Through the principle of separation of variables, the assumed solution $\mathbf{x}(t)$ of the system can be expressed as a product of a time-independent (complex) *shape* vector and a function of time: $\mathbf{x}(t) = \boldsymbol{\phi} e^{st}$. Here, the exponential function of complex variable $s = \alpha + i\beta$ characterises the dynamics of the system (oscillation, i.e. frequency and decay), while $\boldsymbol{\phi}$ conveys the relative spatial information (amplitudes) of the DoFs.

The assumed solution along with its time-derivatives is substituted into the homogeneous EOM, and upon rearranging and collecting common terms a homogeneous equation is obtained involving the product of the assumed solution and a quadratic polynomial matrix in the complex variable s. Since the time-dependent exponent cannot be zero for all t, the solution cannot depend on the time variable, resulting in the nonlinear eigenvalue problem

$$\overbrace{\left(s^2\mathbf{M}_s + s\mathbf{C}_s + \mathbf{K}_s\right)}^{\mathbf{Q}(s)}\boldsymbol{\phi} = \mathbf{0} \tag{2}$$

The spatial solution $\boldsymbol{\phi} = 0$ reflects the trivial case where the system is at rest and is, therefore, of no interest for analysing dynamics. Hence, to satisfy Eq. 2 the quadratic polynomial matrix $\mathbf{Q}(s)$ must be singular, which requires its determinant to be zero. Expanding $\det\mathbf{Q}(s) = 0$ yields a characteristic polynomial with roots s that must be solved by seeking all combinations of complex eigenvalues s and non-zero eigenvectors $\boldsymbol{\phi}$ that satisfy the quadratic problem above. The eigensolution itself and the method of solving it depends on the properties of the damping matrix $\mathbf{C}_s$. In most numerical structural dynamics problems the system is taken to be undamped, i.e. $\mathbf{C}_s = \mathbf{0}$. This assumption simplifies the nonlinear problem in Eq. 2 to a linear generalised eigenproblem of two system matrices, $\mathbf{M}_s$ and $\mathbf{K}_s$:

$$\lambda_n \mathbf{M}_s \boldsymbol{\phi}_n = \mathbf{K}_s \boldsymbol{\phi}_n \qquad n = 1, 2, ..., N \tag{3}$$

$$\text{with} \quad \lambda_n = -s_n^2 = \omega_n^2, \qquad s_n,\ s_n^* = \pm i\omega_n, \qquad \omega_n = \sqrt{\frac{k_n}{m_n}} \tag{4}$$

In the eigenvalue problem of the undamped case has N real-valued generalised eigenvectors $\boldsymbol{\phi}_n$ and corresponding eigenvalues λ_n. From the definition $\lambda = -s^2$ follows that s is purely imaginary for the case $\mathbf{C}_s = \mathbf{0}$ and comes in conjugate pairs, $s, s^* = \pm i\omega_n$; hence the problem above has N complex conjugate pairs of solutions in s_n and N real-valued solutions in λ_n (and by extension ω_n). By assembling all the eigenvectors into columns the generalised modal matrix $\boldsymbol{\Phi}$ is obtained, which has orthogonality properties w.r.t the mass and stiffness matrices [11]:

$$\boldsymbol{\Phi}^{\mathrm{T}}\mathbf{M}_s\boldsymbol{\Phi} = [\diagdown m_n \diagdown] \equiv \mathbf{M}_q, \qquad \boldsymbol{\Phi}^{\mathrm{T}}\mathbf{K}_s\boldsymbol{\Phi} = [\diagdown k_n \diagdown] \equiv \mathbf{K}_q \tag{5}$$

where $\mathbf{M}_q$ and $\mathbf{K}_q$ are the diagonal generalised modal mass and stiffness matrices. The solution to the eigenvalue problem in the form of the eigenvalues and eigenvectors, provides an insight into the inherent dynamical properties of the system. Knowledge of system dynamics can be used to analyse the response of the system to known initial conditions or external excitation. The orthogonality properties of the modal matrices are extremely valuable in modal analysis in that they can be used to decouple the forced EOM by diagonalising the system matrices,

through which the system is coupled. The complete set of generalised eigenvectors $\boldsymbol{\Phi}_n$ form a natural basis (eigenbasis) for $\mathbb{R}^N$ — a linearly independent set that spans the N-dimensional vector space in which the solution $\mathbf{x}$ of the system exists at any time t. Consequently, any vector $\mathbf{x}$ in this vector space can be represented as a superposition of the sum of the eigenbasis vectors:

$$\mathbf{x} = \sum_{n=1}^{N} \boldsymbol{\Phi}_n q_n = \boldsymbol{\Phi}\mathbf{q} \tag{6}$$

where $\mathbf{q}$ is the vector of modal coordinates q_n associated with the n^{th} mode. The matrix expression above represents a coordinate transformation from spatial coordinates $\mathbf{x}$ to modal coordinates $\mathbf{q}$ through the transformation matrix $\boldsymbol{\Phi}$. The coordinate transformation above is also known as the modal decomposition of the response [13], as the response is decomposed/expanded as a superposition of its natural modes. Applying the coordinate transformation and pre-multiplying both sides of the EOM by the transpose of the modal matrix, allows leveraging the orthogonality properties, resulting in a decoupled set of equations of motion:

$$\mathbf{M}_s\ddot{\mathbf{x}}(t) + \mathbf{K}_s\mathbf{x}(t) = \mathbf{F}(t) \quad \Rightarrow \quad \boldsymbol{\Phi}^{\mathrm{T}}\mathbf{M}_s\boldsymbol{\Phi}\ddot{\mathbf{q}}(t) + \boldsymbol{\Phi}^{\mathrm{T}}\mathbf{K}_s\boldsymbol{\Phi}\mathbf{q}(t) = \boldsymbol{\Phi}^{\mathrm{T}}\mathbf{F}(t) \quad \Rightarrow \tag{7}$$

$$\Rightarrow \quad \mathbf{M}_q\ddot{\mathbf{q}}(t) + \mathbf{K}_q\mathbf{q}(t) = \mathbf{f}_q(t) \quad \text{or} \quad m_n\ddot{q}_n(t) + k_n q_n(t) = f_n(t) \quad n = 1,\ 2, \ldots N \tag{8}$$

Here, $\mathbf{f}_q(t) = \boldsymbol{\Phi}^{\mathrm{T}}\mathbf{F}(t)$ is the vector of generalised modal forces signifying the influence of the forcing vector components on each mode. In practice, the spatial matrices obtained from FEM analyses are large and computationally costly. It does little for accuracy to include all modes into the analysis. It is therefore the norm to truncate the columns of the modal matrix as to include a smaller set of modes in which the higher frequency modes are omitted omitted ($\bar{\boldsymbol{\Phi}} \subseteq \boldsymbol{\Phi}, \bar{N} \ll N$). As a result, the overall size of the problem in Eq. 8 is smaller than that of the problem in Eq. 1, effectively representing a modal reduced order model (ROM). Consequently the dimension of the vector of modal forces is significantly smaller than the physical forcing vector of the full order problem.

2.3 Aerodynamics

To investigate dynamic aeroelastic phenomena unsteady aerodynamic models are needed. The *unsteadiness* refers to the degree in which the aerodynamic loads depend on the time variable. The model accuracy of the various available unsteady aerodynamic models depends on whether the numerical model is able account for compressibility and viscosity effects. This study considers two aerodynamic models:

1. ZONA6 Linear Subsonic Unsteady Aerodynamics [14] — is an unsteady panel method developed by ZONA Technology, Inc. for the ZAERO software system. ZONA6 uses a higher-order panelling scheme than the doublet-lattice method (DLM). DLM is a higher-order unsteady flow extension of the low-order vortex-lattice method (VLM), which is a steady panel method. ZONA6 is a higher-order method than DLM as it uses a higher-order polynomial approximation for the representation of the doublet distribution requiring a smaller number of aerodynamic boxes in order to achieve a converged unsteady solution [14] [15].
2. Nonlinear, time-domain, unsteady Computational Fluid Dynamics (CFD) method for 3D viscous, compressible flows. CFD flow models for viscous flows are all based on solving the Navier-Stokes (NS) equations, which total five or four depending on the the compressibility assumptions. Since no close form solution exists, the equations are solved

through approximations. One particular simplification method is Reynolds decomposition, whereby the flow velocity vector field is decomposed into (time-averaged, stationary) mean flow and (time-dependent) fluctuating flow components. After substituting the decomposed velocity vector into the continuity and momentum equations and subsequent ensemble averaging, the fluctuating terms in the continuity equation vanish, while their products are retained in the momentum equation. These Reynolds stresses are turbulent flow fluctuations in fluid momentum; they cannot be resolved and require additional turbulence modelling to close the problem. The (Unsteady) Reynolds-Averaged Navier-Stokes ((U)RANS) flow model is the current industry standard in CFD for mildly separated turbulent flows.

For the purpose of further discussion, the aerodynamic force generated on a structure can be defined as a nonlinear function of flow conditions (i.e. angle-of-attack α, dynamic pressure q_∞, Mach number M_∞ and Reynolds number Re_∞) and time-dependent structural states (encompassing rigid body displacements and flexible deformations):

$$\mathbf{F}_{\text{a}}(t) = \mathbf{F}_{\text{a}}(\{q_\infty, \alpha,\ M_\infty,\ Re_\infty\};\ \ddot{\mathbf{x}}(t), \dot{\mathbf{x}}(t), \mathbf{x}(t)) \tag{9}$$

The degree of unsteadiness and nonlinearity of the aerodynamic forcing function depends on the ability of the chosen flow model to capture the dependency of the aerodynamics on higher-order time derivatives of the structural states.

2.4 Aeroelastic Model

A flexible structure exposed to moving airflow experiences phenomena resulting from a strong interaction between the kinetic and elastic restoring forces on the structure and the dynamics of the surrounding air. An unrestrained flexible structure under loading will exhibit elastic deformation in addition to rigid-body motion. The motion and deformation of the structure will inevitably affect the pressure distribution in the flow, generating aerodynamic forces that in turn affect the response of the structure. These feedback interactions enable motion-induced dynamic behaviour.. The unsteady aeroelastic equations of motion are derived by combining linear structural dynamics and unsteady, structural state-dependent aerodynamics:

$$\mathbf{M}_s\ddot{\mathbf{x}}(t) + \mathbf{C}_s\dot{\mathbf{x}}(t) + \mathbf{K}_s\mathbf{x}(t) = \underbrace{\mathbf{F}_{\text{a}}(\mathcal{F};\ \mathbf{X}(t)) + \mathbf{F}_{\text{ext}}(t)}_{\mathbf{F}(x,t)} \tag{10}$$

The flow conditions are denoted by the set $\mathcal{F} = \{q_\infty, \alpha,\ M_\infty,\ Re_\infty\}$; the semicolon indicates that the problem is considered for a fixed set of flow parameters, hence for a given set $\mathcal{F}$, the aerodynamic forces are assumed to depend on the structural states. The forcing vector $\mathbf{F}_{\text{a}}(\mathcal{F}; \mathbf{X}(t))$ is the vector of motion-induced generalised unsteady aerodynamic forces – a nonlinear function of structural states. Vector $\mathbf{F}_{\text{ext}}(t)$ represents other motion-independent external forces acting on the structural system which may be aerodynamic or stem from other external sources. A shorthand notation $\mathbf{X}(t) :\ \{\mathbf{x}(t),\ \dot{\mathbf{x}}(t),\ \ddot{\mathbf{x}}(t)\}$ is used to convey the nonlinear state-dependency of the aerodynamic forcing function . The notation can be transformed from physical to modal coordinates using the modal expansion in Eq.7, .i.e. $\mathbf{X}(t) = \mathbf{\Phi}\mathcal{Q}(t)$, where the set $\mathcal{Q}(t) : \{\mathbf{q}(t),\ \dot{\mathbf{q}}(t),\ \ddot{\mathbf{q}}(t)\}$. Since the aerodynamic forcing vector is a function of all degrees-of-freedom $\mathbf{x}(t)$ (and its time derivatives), and this dependency extends to each of its individual components, we can state, using the modal shorthand notation, that it is a function of the superposition of *all* modes, $\mathbf{F}_{\text{a}}(\mathcal{F};\ \mathbf{X}(t)) = \mathbf{F}_{\text{a}}(\mathcal{F};\ \mathbf{\Phi}\mathcal{Q}(t))$.

The aeroelastic equation of motion in Eq. 10 represents a closed-loop system, as schematically represented in Fig. 3.

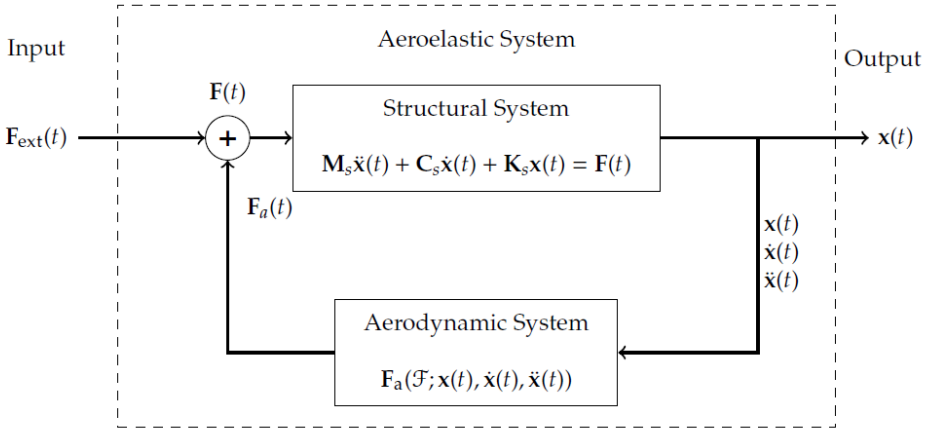

Figure 3: Schematic of an aeroelastic feedback system, represented by Eq. 10.

The dependence of the aerodynamics on the structural states and the subsequent effect on the structural motion forms the feedback loop. The equation of motion in Eq. 10 represents a closed-loop system, as schematically idealised in Fig. 3. The dependence of the aerodynamics on the structural states and the subsequent effect on the structural motion forms the feedback loop. The *structural system* takes the total force $\mathbf{F}(t)$ as input and outputs the structural states (generalised displacements, velocities and accelerations) through the governing equation of motion. The output of the structural system serves as an input to the *aerodynamic system* which outputs a force component that is linearly combined with the external force input and subsequently fed into the structural system. Note that Eq.10 is coupled through the structural system matrices. Based on the earlier discussion on structural dynamics, the structural damping can be neglected. Through coordinate transformation from physical to modal coordinates, and subsequent pre-multiplication of the aeroelastic EOM by the transpose of the modal matrix, the orthogonality of the modal eigenbasis w.r.t. the mass and stiffness matrices can be used to decouple the system of equations in Eq.10. The decoupled aeroelastic matrix equation of motion, yields

$$\mathbf{M}_q\ddot{\mathbf{q}}(t) + \mathbf{K}_q\mathbf{q}(t) = \underbrace{\mathbf{\Phi}^{\mathrm{T}}\mathbf{F}_{\mathrm{a}}(\mathcal{F};\ \mathbf{X}(t))}_{\mathbf{Q}(\mathcal{F};\ \mathbf{X}(t))} + \mathbf{\Phi}^{\mathrm{T}}\mathbf{F}_{\mathrm{ext}}(t) \tag{11}$$

The generalised modal unsteady aerodynamic force vector $\mathbf{Q}(\mathcal{F};\ \mathbf{X}(t))$ represents the modal projection of the generalised unsteady aerodynamic force $\mathbf{F}_{\mathrm{a}}(\mathcal{F};\ \mathbf{X}(t))$. The components of the modal force vector each represent a linear combination of the components of the unsteady aerodynamic force vector; the n^{th} modal force element expresses how much each and every component of the aerodynamic force vector contributes to the excitation of the structural normal mode associated with mode shape $\mathbf{\Phi}_n$.

Let us consider the case of a single-mode excitation, where the structure is forced to deform into its j^{th} mode shape. Hence, $q_n(t) = 0$ for $n \neq j$. According to the modal expansion theory, the response then equals

$$\mathbf{x}(t) = \sum_{n=1}^{N} \mathbf{\Phi}_n q_n(t) = \mathbf{\Phi}_j q_j(t) \tag{12}$$

Substituting the expression into the equation of motion yields the following expression:

$$\mathbf{M}_s \boldsymbol{\Phi}_j \ddot{q}_j(t) + \mathbf{K}_s \boldsymbol{\Phi}_n q_n(t) = \underbrace{\mathbf{F}_{\mathrm{a}|j}(\mathcal{F}; \boldsymbol{\Phi}_j \mathcal{Q}_j(t)) + \mathbf{F}_{\mathrm{ext}|j}(t)}_{\mathbf{F}_j(t)} \tag{13}$$

Since modes $n \neq j$ are not present in the motion, there is no interaction between the modes and the coupled terms within the nonlinear forcing function vanish. LHS is of this equation is known – we know the system matrices from Finite Element Analysis (FEA), and subsequent structural modal analysis gives us the modal matrices containing the eigenvalues and the corresponding eigenvectors per vibration mode. What we seek to identify is the RHS, the *aerodynamic response* to the structural mode n. In this context, the aerodynamics can be viewed as an isolated nonlinear system – one that takes inputs and gives outputs. The loads that develop on the structure are first and foremost caused by the fact that there is an aerodynamic shape in a moving flow and that shape is moving or deforming. The feedback from the aerodynamic loads that subsequently develop is what causes that shape to deform. So if we can prescribe the change in structural shape in a convenient manner, we can effectively decouple the aerodynamic feedback loop. This leaves us with a single system (aerodynamics) that takes a prescribed structural deformation (change in shape) as an input and gives the induced aerodynamic loading as an output. This process is schematically shown in Fig. 4. Note that, as opposed to the fully-coupled aeroelastic system in Fig. 3, the forced modal vibration strategy uses an open-loop approach where the structural motion is prescribed such that the aerodynamics induced by this motion can be characterised without requiring a full two-way fluid-structure coupling. By isolating the

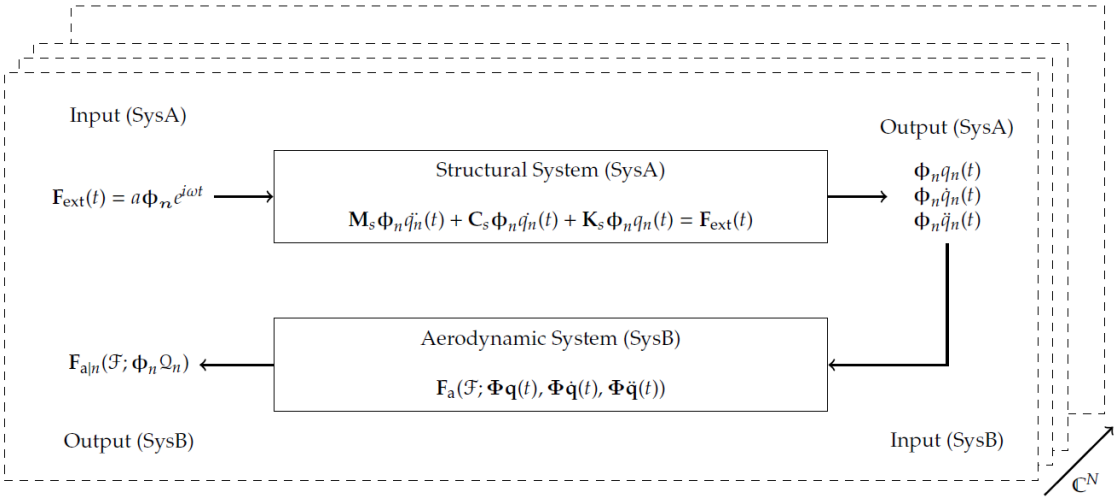

Figure 4: Schematic of an aeroelastic system under forced vibration, represented by Eq. 13.

aerodynamic system, we can investigate the nonlinear relationship between that system's inputs and outputs. The most convenient way of analysing the problem is by considering the Laplace transform (with zero initial conditions) of the nonlinear generalised aerodynamic forcing function:

$$\mathcal{L}\{\mathbf{F}_{\mathrm{a}}(\mathcal{F}; \ddot{\mathbf{x}}(t), \dot{\mathbf{x}}(t), \mathbf{x}(t))\} = \mathbf{F}_{\mathrm{a}}(\mathcal{F}; \mathbf{x}(s), s\mathbf{x}(s), s^2\mathbf{x}(s)) = \mathbf{F}_{\mathrm{a}}(\mathcal{F}; s, \mathbf{x}(s)) \tag{14}$$

Here, $\mathbf{F}_{\mathrm{a}}(\mathcal{F}; s, \mathbf{x}(s))$ is the generalised aerodynamic function in complex frequency domain; it is a nonlinear function of generalised structural states $\mathbf{x}(s)$ and and the complex variable s, signifying its dependence on the time-derivatives of the structural states. It can be viewed as a nonlinear transfer function that takes $\mathbf{x}(s)$ and s as inputs and produces a generalised aerodynamic force vector as an output. Using linearisation methods, the input-output relationship can

be written in the LTI form:

$$\mathbf{H}_{\mathrm{a}}(\mathcal{F}; s, \mathbf{x}(s)) \overset{\text{linearisation}}{\approx} q_\infty \mathbf{H}_a(s)\mathbf{x}(s) \tag{15}$$

where $q_\infty \mathbf{H}_a(s)$ is the linearised aerodynamic transfer function, as a function of complex frequency s – a transfer function that maps inputs from structural deformation, $\mathbf{x}(s)$, into linearised aerodynamic forces, $\mathbf{F}_{a|\mathrm{lin}}(s)$, for a varying s.

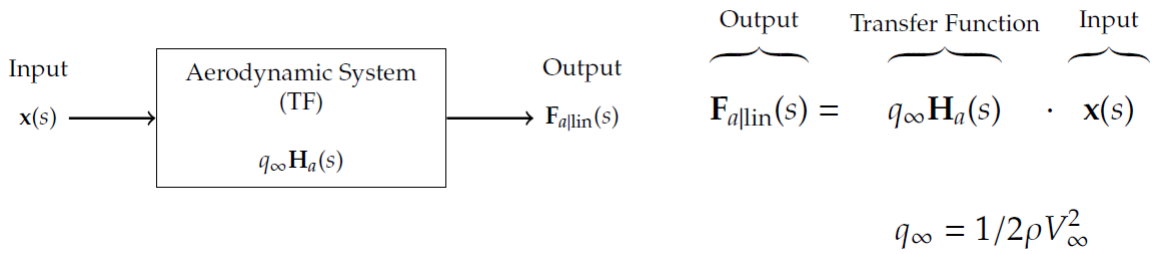

Now that there is a linearised definition for the deformation-induced generalised aerodynamic force in complex frequency domain, it can be substituted into the equation of motion. Performing coordinate transformation, pre-multiplying the equations by the transpose of the modal matrix and taking the Laplace transform of the structural system, yields the decoupled aeroelastic EOM in modal coordinates with linearised aerodynamics in Laplace domain is:

$$\underbrace{\left(s^2\mathbf{M}_q + \mathbf{K}_q\right)}_{[\mathbf{H}_n(s)]^{-1}} \mathbf{q}(s) = q_\infty S \underbrace{\frac{1}{S}\mathbf{\Phi}^{\mathrm{T}}\mathbf{H}_a(s)\mathbf{\Phi}}_{\mathbf{Q}_{\mathrm{GAF}}(s)} \mathbf{q}(s) + \mathbf{\Phi}^{\mathrm{T}}\mathbf{F}_{\mathrm{ext}}(s) \tag{16}$$

Here, the matrix $\mathbf{Q}_{ij}^{\mathrm{GAF}}(s)$ is the q_∞-normalised modal aerodynamic transfer function known as the Generalised Aerodynamic Force (GAF) matrix. The diagonal matrix $\mathbf{H}_n(s)$ is the modal transfer function of the structural system and relates to the structural transfer function $\mathbf{H}(s) = \mathbf{\Phi}\mathbf{H}_n(s)\mathbf{\Phi}^{\mathrm{T}}$. Equation 16 in time domain, yields:

$$\mathbf{M}_q\ddot{\mathbf{q}}(t) + \mathbf{K}_q\mathbf{q}(t) = \underbrace{q_\infty S\mathbf{Q}_{\mathrm{GAF}}(t)}_{\mathbf{\Phi}^{\mathrm{T}}\mathbf{F}_{\mathrm{a}}(\mathcal{F};\ \mathbf{X}(t))} + \mathbf{\Phi}^{\mathrm{T}}\mathbf{F}_{\mathrm{ext}}(t) \tag{17}$$

where

$$\mathbf{Q}_{\mathrm{GAF}}(t) = \frac{1}{S}\mathbf{\Phi}^{\mathrm{T}}\mathbf{F}_{\mathrm{a}}(\mathcal{F};\ \mathbf{X}(t)) \tag{18}$$

Here, S is the reference area, $q_\infty = 1/2\rho V_\infty^2$ is the dynamic pressure, ρ is the air density, and V_∞ the free-stream velocity. The aerodynamic the generalised unsteady aerodynamic force vector $\mathbf{F}_{\mathrm{a}}(\mathcal{F};\ \mathbf{X}(t))$. It should be noted that the DoF indicates the structural grid points. Generally both translational and linear rotational degrees-of-freedom are included in the analysis, which brings the number of DoF to a 6-fold of the number of selected grid points (analysis set, or *a-set*). Upon performing modal analysis, only a small selection of most dominant modes is chosen, yielding a reduced order model (ROM) of the full system.

Since the aerodynamic grid differs from the finite element (FEM) structural grid, additional linear transformation is required to project the FEM coordinates and displacement onto the computational aerodynamic grid; and, in case of a two-way coupling, another transformation

to map the aerodynamic loads onto the structural grid. The fluid-structure interaction (FSI) interpolation conditions are a) kinematic interface condition whereby the interface displacement of the fluid equals the interface displacement of the structure:

$$\mathbf{x}_f = \mathbf{x}_s \overset{\text{Discretization}}{\rightarrow} \mathbf{X}_f = \mathbf{H}_{sf}\mathbf{X}_s \tag{19}$$

and b) dynamic interface condition, whereby the forces at the structure interface equal the forces at the fluid interface

$$\mathbf{p}_s\mathbf{n}_s = \mathbf{p}_f\mathbf{n}_f \overset{\text{Discretisation}}{\rightarrow} \mathbf{P}_s = \mathbf{H}_{fs}\mathbf{P}_f \tag{20}$$

$\mathbf{H}_{sf}$ and $\mathbf{H}_{fs}$ are transformation matrices and can be defined using consistent and conservative approaches. A consistent approach requires the row sum of the transformation matrices to be zero; a conservative approach requires virtual work on the structural mesh to equal the work on fluid mesh, thereby conserving the energy transfer over the fluid-structure interface. For forced vibration analysis only the first condition is of interest.

3 COMPUTATIONAL METHODOLOGY AND ANALYSES

The primary goals of this study were to: a) determine the Generalised Aerodynamic Forces (GAFs) using a high-fidelity RANS-based computational aeroelastic simulation); b) compare the results to aeroelastic simulations using a lower fidelity aerodynamic panel method model; c) provide the simulation results to the AePW-3 Flight Test Working Group for comparison with the low and high-fidelity simulations performed by other members.

To achieve these goals a series of structural, aerodynamic and aeroelastic analyses and methods were implemented. This section discusses the linear structural dynamics analyses performed in NASTRAN based on the input data provided to the AePW-3 Flight Test Working Group participants for one of the four X-56A models. Two computational aerodynamics and aeroelastics tools and methods were used in this study to generate the Generalised Aerodynamic Forces and analyse the flutter behaviour. Namely, the ZAERO flow system [14, 16] from ZONA Technology, Inc. using a higher-order panel method (ZONA6) [14], and the computational fluid dynamics (CFD) simulation system ENFLOW for multi-block flow domains developed by the Netherlands Aerospace Centre (NLR) based on the Reynolds-Averaged Navier-Stokes (RANS) flow equations [17–20]. The procedure for the ENSOLV CAE simulations is presented at the end of this chapter.

3.1 NASTRAN — Linear Structural Dynamic Analysis

The AePW-3 Flight Test Working Group was provided with in total four fuel state configurations, 10lb, 30lb, 60lb and 80lb. Given the computational cost associated with CFD-based aeroelastic simulations, only one fuel state was considered in the CAE simulations, namely the 10lb fuel case.

The full NASTRAN FEM model has in total 12333 elements, i.e. shell (QUAD4/TRIA3), beam (LINE2) geometry (POINT) and solid (PENT6/HEXA8). There are in total 8480 nodes and 50880 DoFs, which is the number of nodes multiplied by 3 translational DoFs + 3 rotational DoFs per node. A reduced analysis set (ASET1) of 407 nodes in 6 DoFs per node was chosen to reduce the size of the problem. A graphic representation of the finite element (FE) model including grid and full set of grid points is given in Fig. 5.

The normal modes were computed using the NASTRAN SOL103 Linear Dynamics solver. In the previous work [8], the eigenvalue extraction method Lanczos was chosen, specified under

the EIGRL Bulk Data entry. For the present study, the extraction method was AHOU, defined under the EIGR Bulk Data entry. The normalisation method (NORM) was chosen as MAX, which normalised the eigenvectors to unit value of the largest displacement in the analysis set. In total 15 modes where requested, of which the first 6 are rigid body and the remaining 9 are flexible modes, these results are summarised in Table 2. The major difference between the two eigenvalue extraction methods is that the present analysis produced 6 *clean* rigid body modes with 3 pure translations and 3 pure rotations, whereas the previous analysis produced rigid body modes that exhibited 6 coupled translational and rotational displacements. More detail about the NASTRAN SOL103 settings can be found in [21].

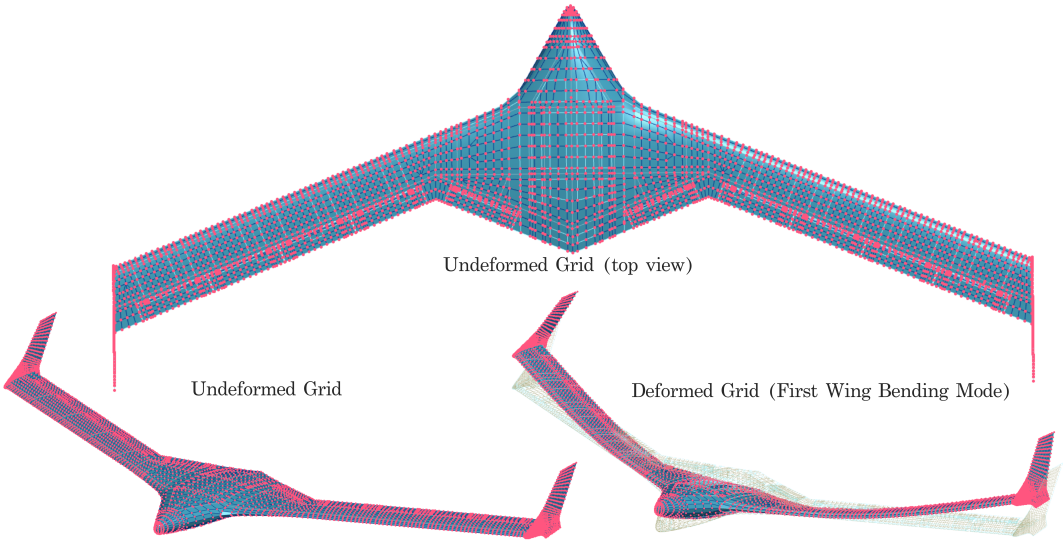

Figure 5: NASTRAN Finite Element model with the full set of nodes (rendered).

Table 2: X-56A 10lb Structural Modes.

	Mode	Notation	Description	f, Hz
Rigid Body Modes (RBM)	1	Ux	Surge	0.000
	2	Uy	Sway	0.000
	3	Uz	Plunge	0.000
	4	Rx	Roll	0.000
	5	Ry	Pitch	0.000
	6	Rz	Yaw	0.000
Flexible Modes (FlexM)	7	SW1B	Symmetric Wing First Bending	3.219
	8	AW1B	Asymmetric Wing First Bending	5.318
	9	SW1T	Symmetric Wing First Torsion	11.160
	10	SWFAB	Symmetric Wing Fore-Aft Bending	12.268
	11	AW1T	Asymmetric Wing First Torsion	13.282
	12	SW2B	Symmetric Wing Second Bending	16.167
	13	AW2B	Asymmetric Wing Second Bending	18.184
	14	AWLB	Asymmetric Winglet Bending	21.120
	15	SWLB	Symmetric Winglet Bending	23.005

3.2 ZAERO — ZONA6 Subsonic Unsteady Panel Method for Aeroelastic Simulations

Within ZAERO the aerodynamic panels are modelled as flat plates which will suffice for the linear flutter approach. A full span model containing 1848 aerodynamic panels is modelled. The generalised aerodynamic forces are computed by ZAERO using its own higher order panel code ZONA6 [14] based on linear potential flow. ZONA6 is a linear subsonic unsteady panel method developed by ZONA Technology, Inc. for the ZAERO software system. ZONA6 uses a higher-order panelling scheme than DLM to achieve improved accuracy and computational efficiency [15].

The ZONA6 aerodynamic panel model for X-56A is created based on the CAD model provided within AePW-3. The aerodynamic panel model is shown in Fig. 6. Besides the fuselage and wings, the body flap, four wing flaps and the winglets are included. The aerodynamic panels are modelled as flat plates which are adequate for the linear flutter approach in Eq. 21. It is a full span model containing 1848 aerodynamic panels. To adequately capture the unsteady aerodynamics, 21 discrete reduced frequencies ($0 \leq k \leq 0.99846$) were considered for each of the 15 modes.

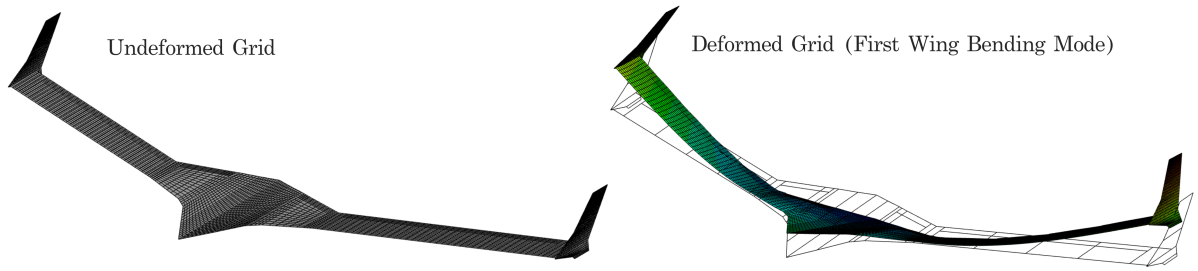

Figure 6: ZAERO: ZONA6 Aerodynamic Model and Grid.

3.2.1 Flutter Analyses

The unsteady analyses result in a the generalised aerodynamic forces (GAFs) denoted by Q_{HH}, required to solve the flutter equation. ZAERO is used to solve for the aeroelastic equation, using its build-in g-method. The GAFs are computed by ZAERO using its own ZONA6 panel code based on linear potential flow. The resulting Q_{HH} data can be replaced by other matrices obtained from other methods, such as CFD-RANS as described before. The flutter equation that is to be solved with the g-method is::

$$\left[\left(\frac{V^2}{L^2}\right)\mathbf{M}p^2 + \mathbf{K} - \frac{1}{2}pV^2\mathbf{Q}'\left(ik\right)g - \frac{1}{2}\rho V^2\mathbf{Q}\left(ik\right)\right]\{\mathbf{q}\} = 0 \tag{21}$$

$$k = \frac{\omega L_z}{2V} \tag{22}$$

where V is the velocity, $L_z = c/2$ is a reference length, $\mathbf{M}$ is the mass matrix, ρ is the density, k is the reduced frequency, $\mathbf{Q}$ and $\mathbf{Q}'$ are the GAFs and the derivative of this matrix, respectively. Finally, p is the non-dimensional Laplace parameter and $\mathbf{q}$ is the mode shape matrix. The method is related to the PK-method which is commonly used in industry. Both methods reduce to the same form when the computed damping is zero, meaning that the both methods compute the same flutter speeds. More on the g-method implemented in ZAERO can be found in [14].

3.3 ENSOLV — (U)RANS Computational Fluid Dynamics/Aeroelastics Simulations

The flow solver ENSOLV, developed by the Netherlands Aerospace Centre (NLR) , offers Computational Fluid Dynamics (CFD) and Computational AeroElastics (CAE) capabilities for high-fidelity aerodynamic and aeroelastic simulations [17, 20]. The solver is part of the NLR's flow simulation system ENFLOW, which in addition to the flow solver consists of a domain modeller and a grid generator. The domain modeller ENDOMO creates the topology description and the geometry of the boundaries of the 3D multi-block flow domain, decomposing it into subdomains called blocks. The grid generator ENGRID constructs the corresponding multi-block structured grid in edges, blocks and block faces. [17, 19].

The high-fidelity CFD and CAE computations where performed using the ENSOLV code that solves the (unsteady) Reynolds-Averaged Navier-Stokes ((U)RANS) equations on a deforming multi-block structured grid generated with ENGRID. The ENSOLV model/grid is shown in Fig. 7. RANS turbulence modelling is implemented via a custom Explicit Algebraic Reynolds Stress Model (EARSM) based on turbulent/non-turbulent (TNT) $k-\omega$ model for determination of the relevant turbulent time and length scales [19, 22] ; this turbulence model provides a more nuanced representation of turbulent flows [23]. Spatial discretisation in the simulations is achieved through a second-order scheme. The time-integration is handled via a 5-stage explicit Runge-Kutta scheme with implicit residual averaging. The X-56A simulation is performed at a low Mach number; to address convergence issues stemming from unsteady simulations for weakly compressible flows, a low-Mach preconditioning is implemented. A summary of the ENSOLV simulation parameters is provided in Table 3 under Sec. 4.

For the CFD and CAE study on the X-56A, the grid generated in ENGRID consists of multi-block, block-structured O-grids. The far field boundaries were extended to approximately 15 semi-spans away from the model to effectively minimise the influence of boundary constraints on the simulated aerodynamics, ensuring sufficient distance to avoid artificial reflections of the flow properties back to the model. The y^+ value of the first cell was ensured to be below 1 to accurately resolve the boundary layer effects near the surface. Multi-grid capabilities were ensured supporting up to three grid levels, for increased convergence rates and reduced computational cost during the simulation process. The X-56 geometry solid surface is modelled with a no-slip boundary condition. Far-field boundaries are all modelled with a general free-stream boundary condition based on Riemann invariants.

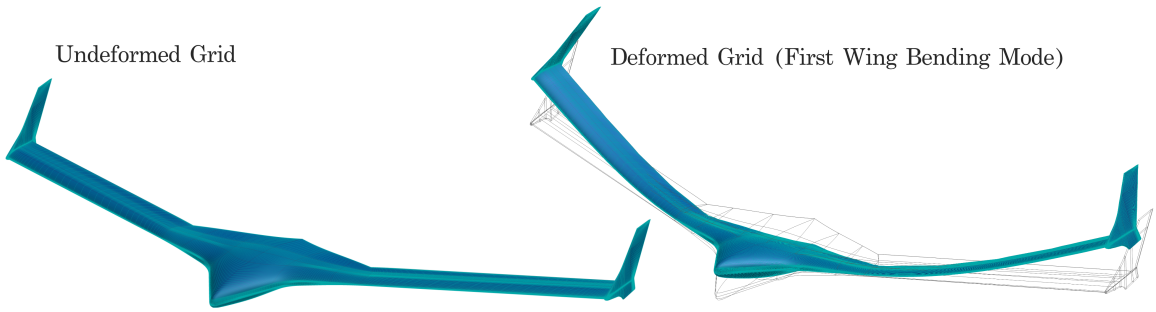

Figure 7: ENSOLV/ENGRID Model: jig shape (left), first flexible mode (right).

3.3.1 Refinement of the CFD/CAE Methodology

After comparing the results produced by the AePW-3 working group, some discrepancies were noticed in the results produced in the previous study [8], especially in the lower reduced frequency range, which became apparent in intermediate AePW-3 working group reviews. Especially when considered on a logarithmic plot, the differences were significant enough to warrant further investigation. The purpose of the present study, was to investigate the cause and address the issues that may have contributed to the problems. GAF results [4],

Firstly, as explained in the discussion in Sec.3.1, the rigid body mode shapes used in the first analysis exhibited coupling between translation and rotational modes. The NASTRAN modal analysis for the present study ensured that the rigid body modes were pure translations and rotation. Secondly, the CFD grid was further investigated and optimised on several accounts. The shape of the trailing edge at the winglet tip was slightly adjusted to eliminate sharp edges and their effect on the quality of the simulations. The far field boundary was extended to 15 semi-spans from the model, whereas the older version of the grid may have been insufficiently suited for particular type of analyses, possibly affecting the flow properties in unsteady simulations. A comprehensive grid convergence study was performed on four grid iterations of increasing refinement. The grid chosen for the present study contains twice as many cells as the older version of the grid. Further optimisation of the CFD/CAE simulations included preconditioning for low-Mach simulations.

In addition to grid optimisation, additional static aeroelastic analyses were performed to determine the flight shape. However, the dynamic CAE analysis were performed on the jig shape, since the flight shape would introduce initial structural condition in addition to the initial aerodynamic condition present due to the steady flow around the undeformed jig shape, which would necessitate additional FEM dynamic analyses to account for the pre-loaded conditions on the flight shape.

3.4 ENSOLV CAE Simulation Procedures

The ENSOLV Computational AeroElastic (CAE) simulation procedure consists of a pre-processing chain, steady CFD analysis, unsteady CFD analyses and a post-processing chain to obtain the GAFs. A flowchart of the process is provided in Fig.8. The high-fidelity CFD and CAE analyses were performed using the ENSOLV code that solves the (unsteady) RANS equations on a deforming multi-block structured grid. The four-phase computational chain consisted of a pre-processing where the structural modes obtained from NASTRAN are projected onto the aerodynamic surface grid through a spatial interpolation scheme; a steady RANS analysis in ENSOLV on the undeformed grid representing the jig shape; an unsteady RANS simulations in ENSOLV using consecutive forced vibrations of the CFD-splined structural modes at different values of reduced frequencies using a 3-period sine-excitation with a small amplitude; and a post-processing chain entailed the transformation of the time-domain GAFs obtained with unsteady aeroelastic simulations to frequency domain. The total number of runs performed in the forced vibration computational chain equalled the number of structural modes multiplied by the number of reduced frequencies of interest. The results obtained from the ENSOLV analyses were compared to those obtained from ZAERO analyses as well as the results provided by other participants of the AePW-3 Flight Test Working Group [4].

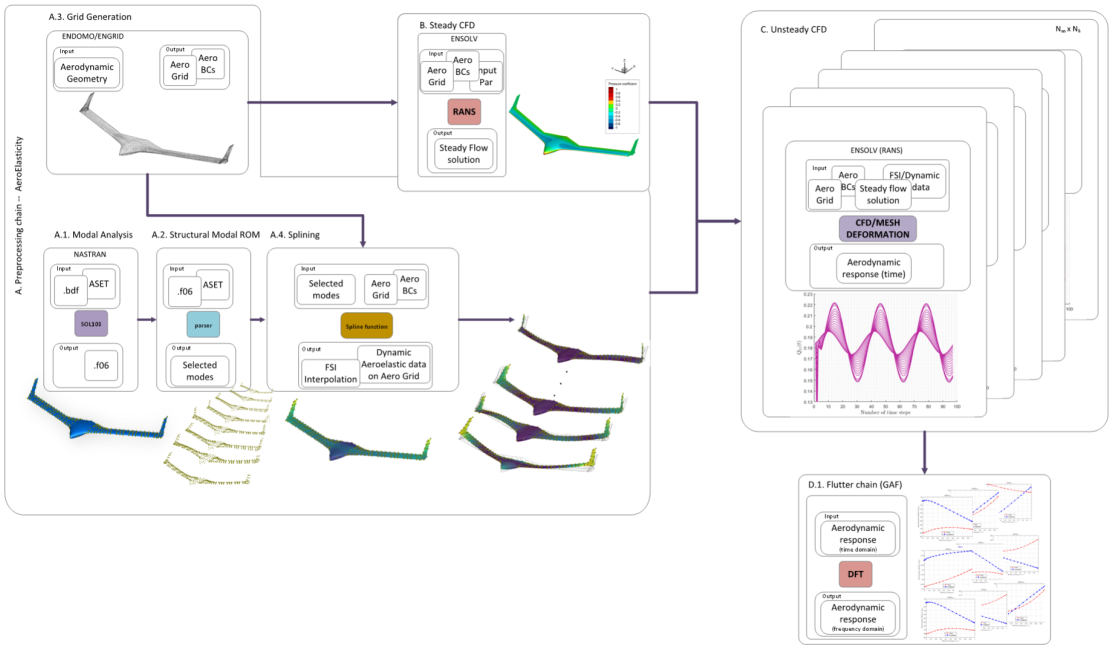

Figure 8: Flowchart of High-Fidelity Computational AeroElastic (CAE) Simulations Chain in ENSOLV.

3.4.1 CAE Preprocessing

The high-fidelity CAE preprocessing chain starts with the computation of finite-element structural modes in NASTRAN (SOL 103) according to methodology discussed in Sec. 3.1. This corresponds to step A.1. of the preprocessing chain shown in Fig. 8. Structural analysis was based on a set of 407 analysis nodes (ASET1) selected such that the modal analysis performed on the reduced set did not diverge form the analysis on the full set for at least the first 15 modes (6 rigid body + 9 flexible modes), as summarised in Table 2. The landing gear modes were discarded.

Subsequently, in step A.2. of the flow chart (Fig. 8) the modal data was extracted from the .f06 NASTRAN output file and restructured to fit the input file structure for the FORTRAN spatial interpolation algorithm which is part of the preprocessing chain for ENSOLV. In a step parallel to the NASTRAN analysis, A.3. of the process chain, the aerodynamic grid is created with ENDOMO flow domain modeller and ENGRID multi-block structured grid generator.

The aerodynamic surface grid and the boundary conditions defining the flow model and the FSI (Fluid-Structure Interaction) interface are used, along with the structural modal data, as inputs for the grid interpolation procedure outlined in step A.4. The output of this step is the interpolation of the structural modes onto the FSI interface defined by the aerodynamic surface grid. The interpolation of the FE structural mode shapes is performed on the jig geometry of X-56A. The results are presented in Sec.4.

3.4.2 Steady CFD Analyses

Within the CAE process chain in ENSOLV, steady analysis corresponds to step B. of the flowchart in Fig. 8. Steady RANS analyses were performed on both the jig shape geometry and the flight shape geometry. The latter was obtained from a static aeroelastic analysis in ENSOLV. The CFD analyses were performed for the conditions provided in Table 3. To address issues

stemming from computing weakly compressible or practically incompressible flows, low-Mach preconditioning is used to improve accuracy and convergence.

Table 3: CFD Simulation Parameters.

M	α	Re	L_{ref} [in]	A_{ref} [in^2]	b [in]
0.151	0 deg	2.1201e+06	24	8064	336
Reference Parameters					
Moment Centre		$[x_{c_M},\ y_{c_M},\ z_{c_M}]$	$[163.5,\ 0.0,\ 104.0]$		in
Moment Arms		$[L_{M_x},\ L_{M_y},\ L_{M_z}]$	[b, c, b]		in

The parameters in Table 3 are: angle-of-attack α, Knots Equivalent Air Speed V_{KEAS}, dynamic pressure q_∞, air density at sea level ρ_0, Mach number M_∞, Reynolds number Re_∞, wing span b, chord length c, characteristic length L_{ref}, and reference wing surface area A_{ref}.

The steady flow solution is used as the initial condition of the unsteady aerodynamic system and is used as an input for the unsteady forced vibrations computations detailed in the next section. Previous work [8] did not include a CFD-based static aeroelastic analysis. The present study has conducted a static CAE simulation to to determine the flight shape. However, within the CAE procedure, the jig shape grid and the corresponding steady solution were used for further unsteady computations. It should be noted, that the context of aeroelastic modelling, the aerodynamic shape used for the steady analysis represents the initial structural state condition (i.e. the baseline shape) for the aeroelastic system as formulated in Sec. 2.4. The corresponding initial aerodynamic force condition is represented by the steady flow solution of the baseline shape. In contrast, the structural modal analysis is logically performed on the jig shape as it is the unloaded jig geometry that defines the initial structural state condition; the system dynamics obtained from modal analysis of the unloaded structure implicitly account for this initial structural state. The situation changes when the flight shape is used in the forced vibration analysis: the flight shape and the corresponding steady flow solution now form a static aeroelastic system, and the modal matrices obtained for the unloaded jig geometry are no longer representative for the dynamics of the (pre-loaded) static aeroelastic state. To implement the flight shape into the CFD forced vibrations analysis, additional steps are required to obtain the dynamic characteristics of the pre-loaded static aeroelastic system defined by the flight shape and the corresponding steady flow solution.

3.4.3 Unsteady CFD Analyses: Forced Vibrations

Unsteady aeroelastic analyses in ENSOLV require the following inputs: steady flow solution representing the initial conditions of the aerodynamics, FSI interpolation and dynamic aeroelastic modal data projected onto the aerodynamic surface grid, the aerodynamic grid and boundary conditions. The procedure is schematically depicted in step C of the flow chart in Fig. 8. The aerodynamic grid used in this study was chosen based on an additional grid refinement process and grid convergence study, presented in Sec. 4.

The type of aeroelastic simulations performed for this case study was a CFD based forced vibration analysis for a set of reduced frequencies. The mathematical background of this simulation was described in Sec. 2.4. A single forced vibration simulation entails the aerodynamic response to a single, prescribed structural mode excitation for a fixed reduced frequency, k_{EN}.

The number of analyses required to obtain the complete GAF matrix equals the number of modes multiplied by the number of reduced frequencies of interest.

4 RESULTS

The results of this study are presented in this section. The overview includes the results of the CFD grid refinement process and the grid convergence study; spatial interpolation of the mode shapes from FE onto CFD grids; evaluation of the static aeroelastic shape (flight shape) compared to the jig shape; the steady flow solutions computed for both the jig shape and the flight shape; the computed GAFs using the two outlined methods (i.e. ZAERO vs. ENSOLV); the flutter diagrams obtained from ZAERO analyses.

4.1 CFD Gird Refinement

The results of the grid refinement efforts and the convergence study are presented here for four different grid iterations, denoted G1 to G4, of increasing refinement ranging from coarse to extra fine. The G1-G4 grids were generated in ENGRID based on the jig shape model. The grids consist of multi-block, block-structured O-grids. Multi-level grid features are implemented, resulting in a multi-grid of 3 refinement levels. The far field boundaries are modelled approximately 15 semi-spans away from the model. The y^+ value of the first cell was ensured to be below 1. Renderings of the surface grids generated by ENGRID, are shown in Fig. 9.

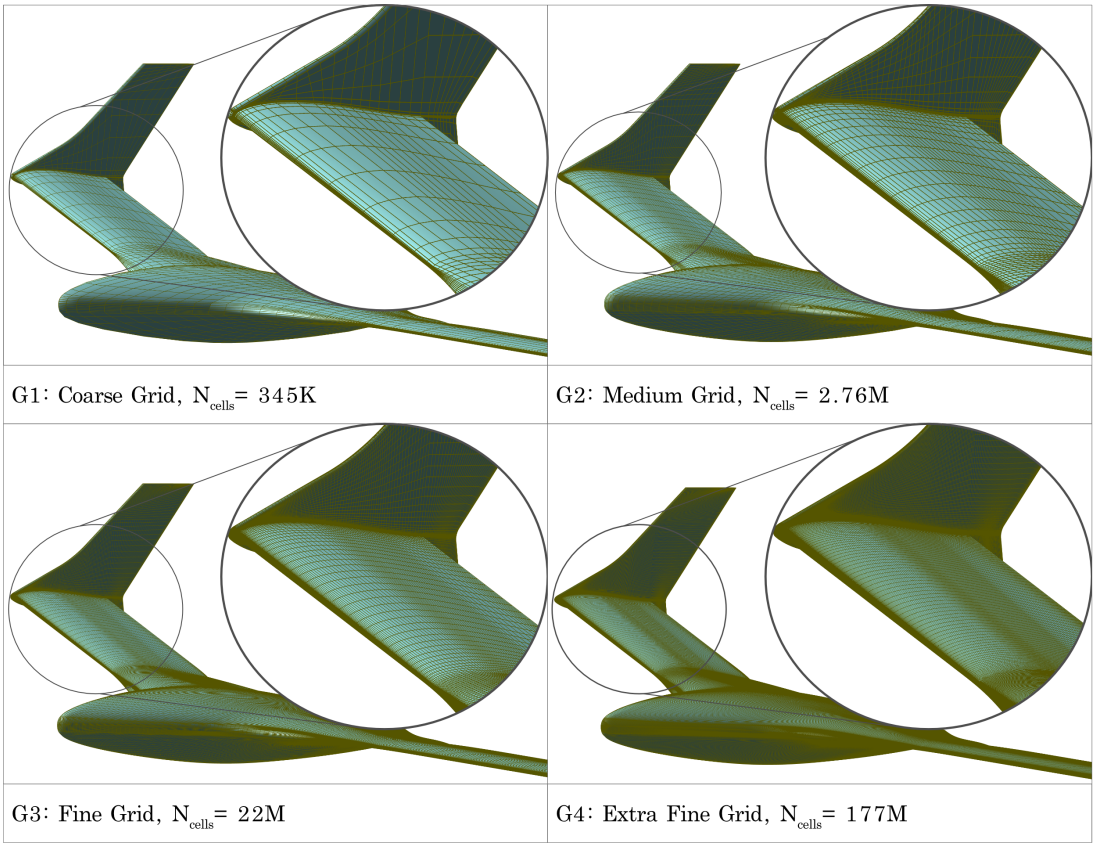

Figure 9: CFD grid iterations and corresponding grid sizes.

The steady RANS analyses were performed in ENSOLV on each grid to investigate the convergence of the aerodynamic lift and drag coefficients, as well as the pitching moment coefficients. The results of the steady analyses for the grid convergence study are summarised in Table 4.

Table 4: Grid convergence study — Steady RANS analyses (full model)

	Grid	Number of Cells	C_L	C_D	C_m
G1	Coarse	345,212	0.779425E-01	0.214457E-01	-0.40706238
G2	Medium	2,761,696	0.835614E-01	0.166607E-01	-0.46682722
G3	Fine	22,093,568	0.859357E-01	0.152009E-012	-0.49040246
G4	XFine	176,748,544	0.870616E-01	0.1474356E-01	-0.500506

It should be noted that the moment centre used here did not correspond to the reference values indicated in Table 3. Instead, a moment centre of $[0.0,\ 0.0,\ 0.0]$ was used for grid convergence studies, beyond which this carries no further significance.

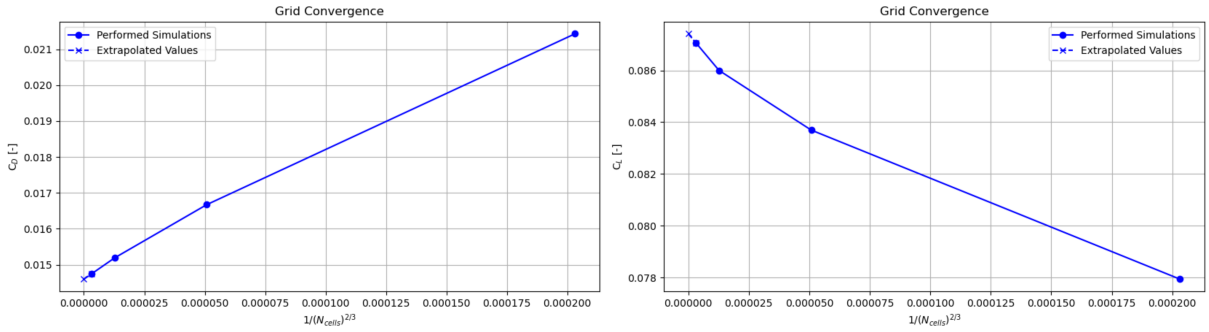

Figure 10: Grid convergence study for C_D and C_L for G1 to G4.

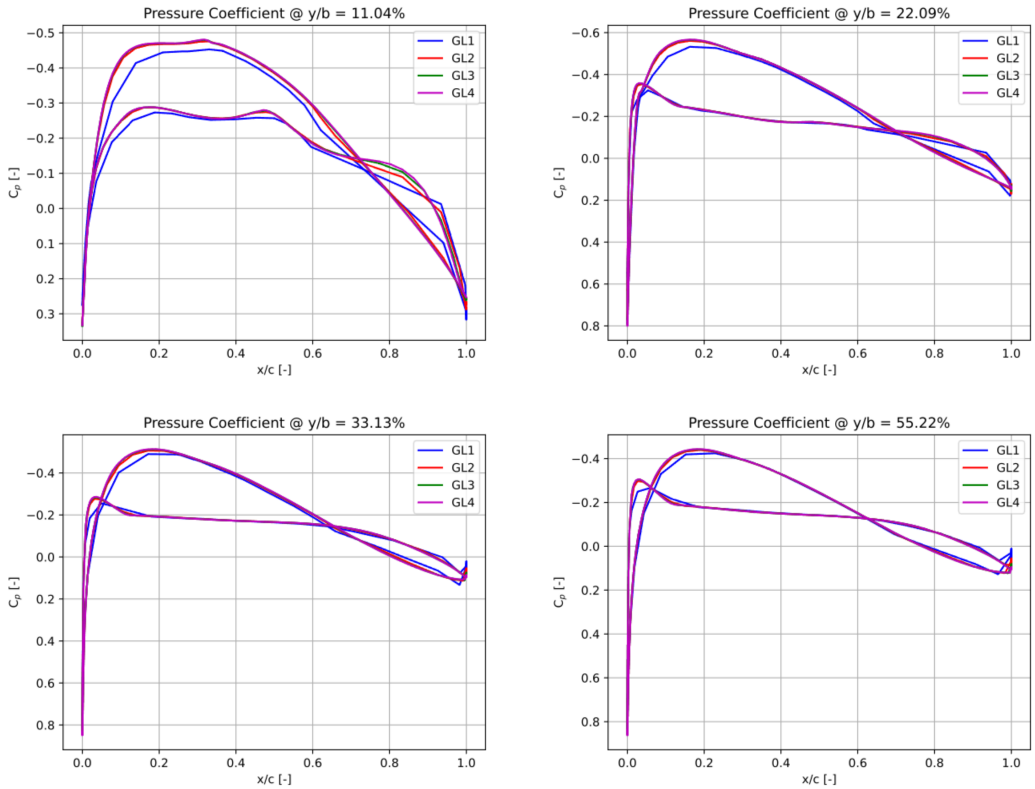

Figure 11: C_p distribution at different span sections, investigated for grid sizes G1 to G4.

Plotting the C_D and C_L values for each grid iteration against the number of grid cells and extrapolating the results showed that the G3 grid converged within 6 drag counts of the extrapolated C_D value and within 2 lift counts of the extrapolated C_L value. The plots are shown in Fig. 10.

Similarly, investigating the pressure coefficient c_p chord distribution at different span sections for the four grid sizes (Fig. 11), shows that the $G1$ and $G2$ grids are insufficient for accurate analyses, while $G3$ is well-converged. Compared to earlier work presented in [8], the CFD grid was further optimised on several accounts, including slight remodelling of the winglet edges and additional extension of the far field boundaries.

The highlighting in Table 4 indicates that grid G3 emerged from the convergence study as the best option and was subsequently used in all analyses presented in this paper.

4.2 Steady CFD/CAE Simulation Results

As discussed in the previous section, the G3 grid (22M cells) emerged as the the best option from the grid convergence study, an was subsequently used for all analyses. G3 grid corresponds to the the X-56A jig shape geometry. G3 computational grid consists of multi-block, block-structured O-grids with 3 refinement levels. The y^+ value of the first is below 1. The far field boundaries are modelled at a distance of 15 semi-spans to eliminate for unsteady simulations.

The multi-level grid enables more efficient computations, whereby the number of iterations can be adjusted per grid level to enable faster convergence. On multi-grid calculations, converged solution was reached within 100 iterations on the finest grid level, starting from a converged solution on the coarser levels. The G3 grid of the full computational fluid domain is illustrated in Fig. 12.

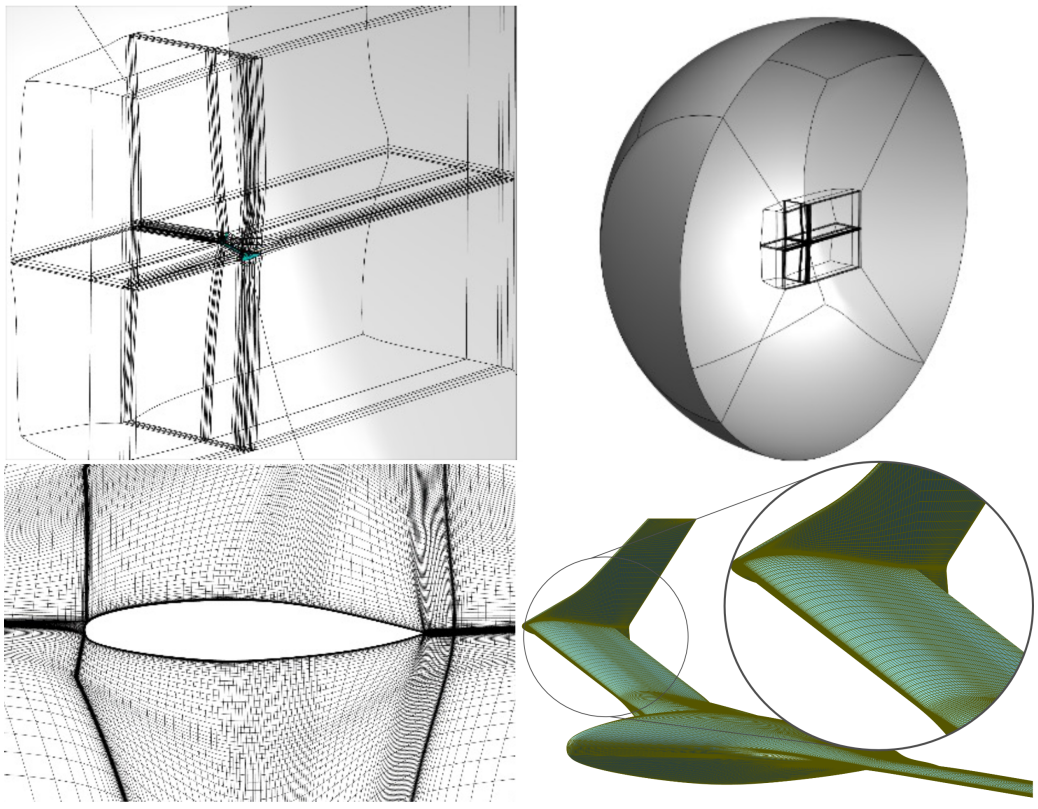

Figure 12: Illustration of the full G3 grid computational fluid domain.

Previous work [8] did not include static aeroelastic simulation. For the present study, additional efforts were undertaken to determine the static aeroelastic shape (flight shape) and investigate the effect of wing tip deflection and twist on the steady RANS simulation in relation to the results obtained for the jig shape. Both shapes are graphically compared in Fig. 13. The static aeroelastic (flight) shape exhibits a tip deflection $d\delta_{\text{tip}}$ of 1.15 inch and an approximate tip incidence angle $d\alpha_{i\text{tip}}$ of 0.92 deg, with respect to the undeformed (jig) shape.

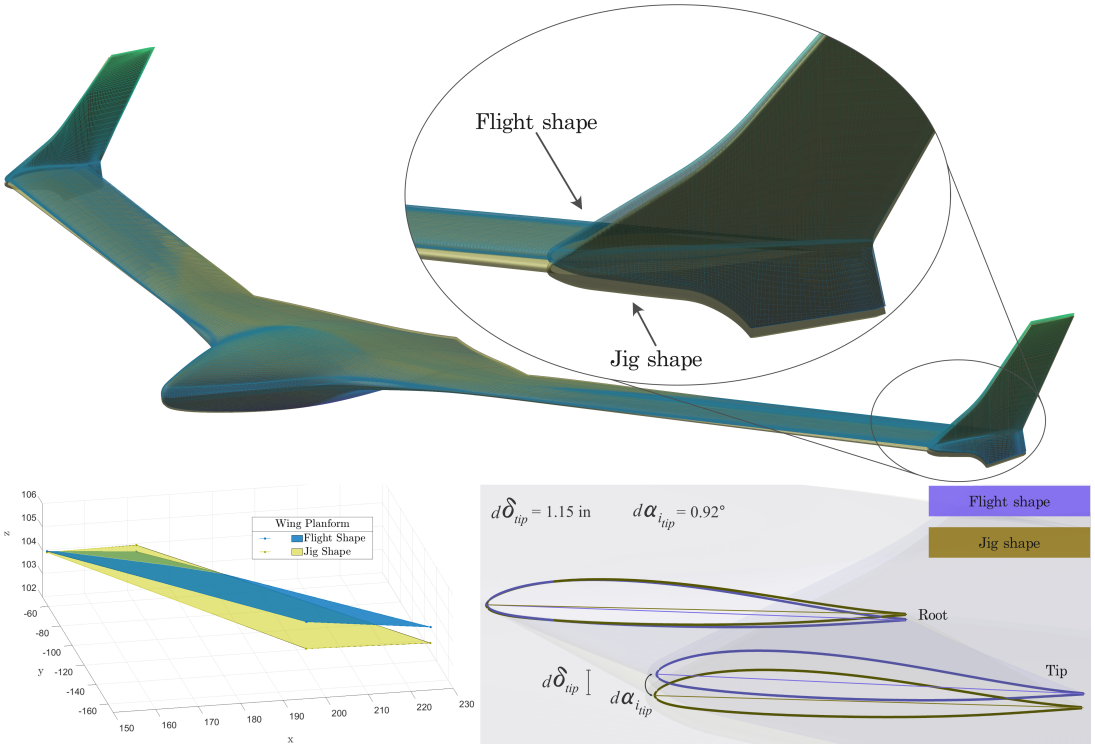

Figure 13: Jig Shape vs. Flight Shape.

The steady RANS results for G3 jig shape and flight shape, are presented below. The flow conditions used for this simulation were summarised in Table 3. The pressure coefficient distribution along the surface is plotted in Fig. 14 for each case. The integrated values of the steady RANS simulations are summarised in Table 5. Despite the seemingly small differences between the flight and jig shape, the steady RANS analyses demonstrate a significant change in C_L values, namely $dC_L = 0.0859$, with the flight shape result nearly twice the value of the jig shape result. However, if we consider the thin airfoil theory, $dC_L = 2\pi d\alpha$, we can conclude that in order to achieve a similar change in C_L for an ideal case, the change in the angle-of-attack must be $d\alpha = 0.0137$ rad $= 0.7833$ deg. Thus, for an idealised wing, even a smaller increase in incidence will be sufficient to cause an equal increase in lift coefficient as determined for the X-56A flight shape.

Table 5: Steady CFD Simulation Static Aeroelastic Shape

	C_L	C_D	C_m
Jig Shape	0.08594	0.01520	0.02972
Flight Shape	0.17180	0.01572	0.02068

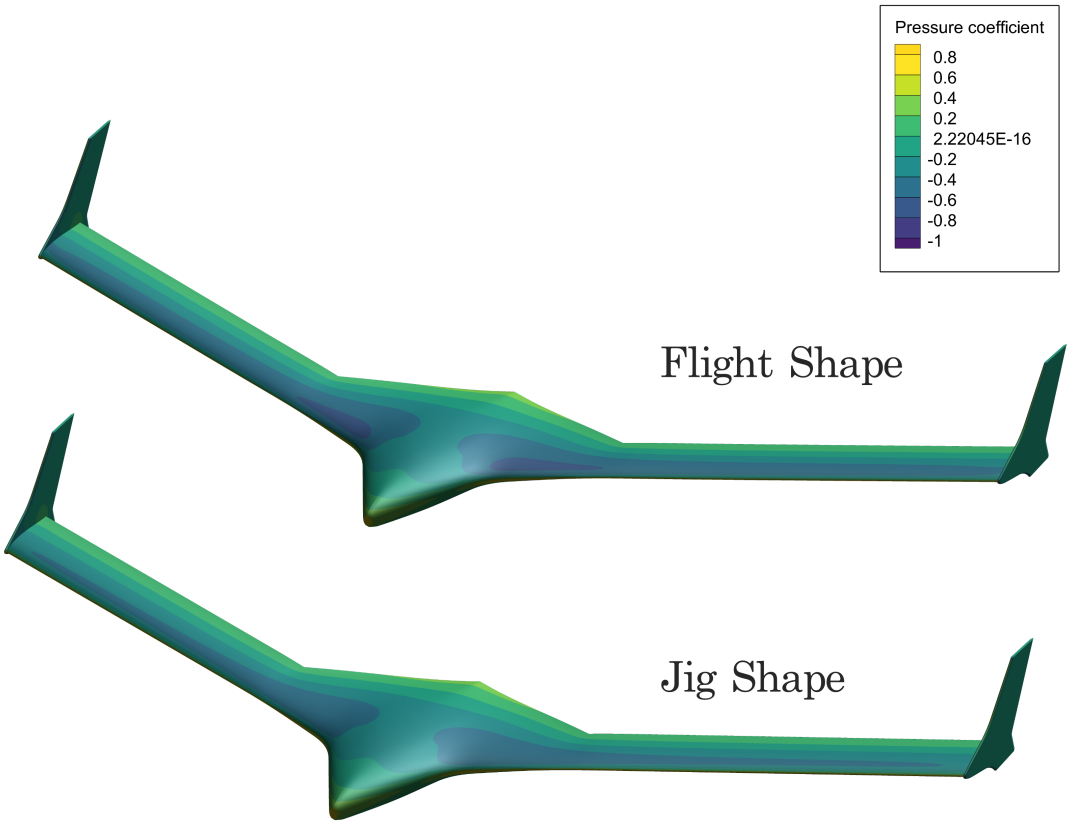

Figure 14: Steady RANS simulation, pressure coefficient distribution – G3 jig vs. flight shape.

4.3 FE/CFD Grid Interpolation for Structural Mode Shapes

In order to perform aeroelastic analyses in a computational fluid dynamics domain, the structural nodes and the corresponding DoFs of the finite element model (NASTRAN) must be projected onto the computational fluid dynamics grid (ENGRID/ENSOLV). Along with the nodal coordinates and boundary conditions, the modal displacement information obtained from linear structural dynamics analysis must be projected as well. In other words, each mode shape obtained from the FE structural analysis needs to be splined onto the aerodynamic grid. This splining process or grid interpolation procedure, is schematically outlined in step A.4. of the preprocessing chain depicted in Fig 8. The output of this step is the interpolation of the structural modes onto the FSI interface defined by the aerodynamic surface grid. The interpolation of the FE structural mode shapes is performed on the jig geometry of X-56A.

Grid interpolation, although only defined as a preprocessing step in the computational chain, is essential for accurate CFD-based aeroelastic simulations and requires careful considerations and effort. An iterative approach is employed, using a combination of intermediate unsteady analyses and graphical evaluation to determine the right interpolation settings and the optimal set of FE analysis nodes to achieve smooth interpolation. For the X-56A model of 15 modes and G3 computational grid, the analysis set (ASET1) of 407 nodes in 3 translational degrees-of-freedom proved sufficient for smooth interpolation. The results are summarised in Figs.15 and 16 for rigid body and flexible modes, respectively.

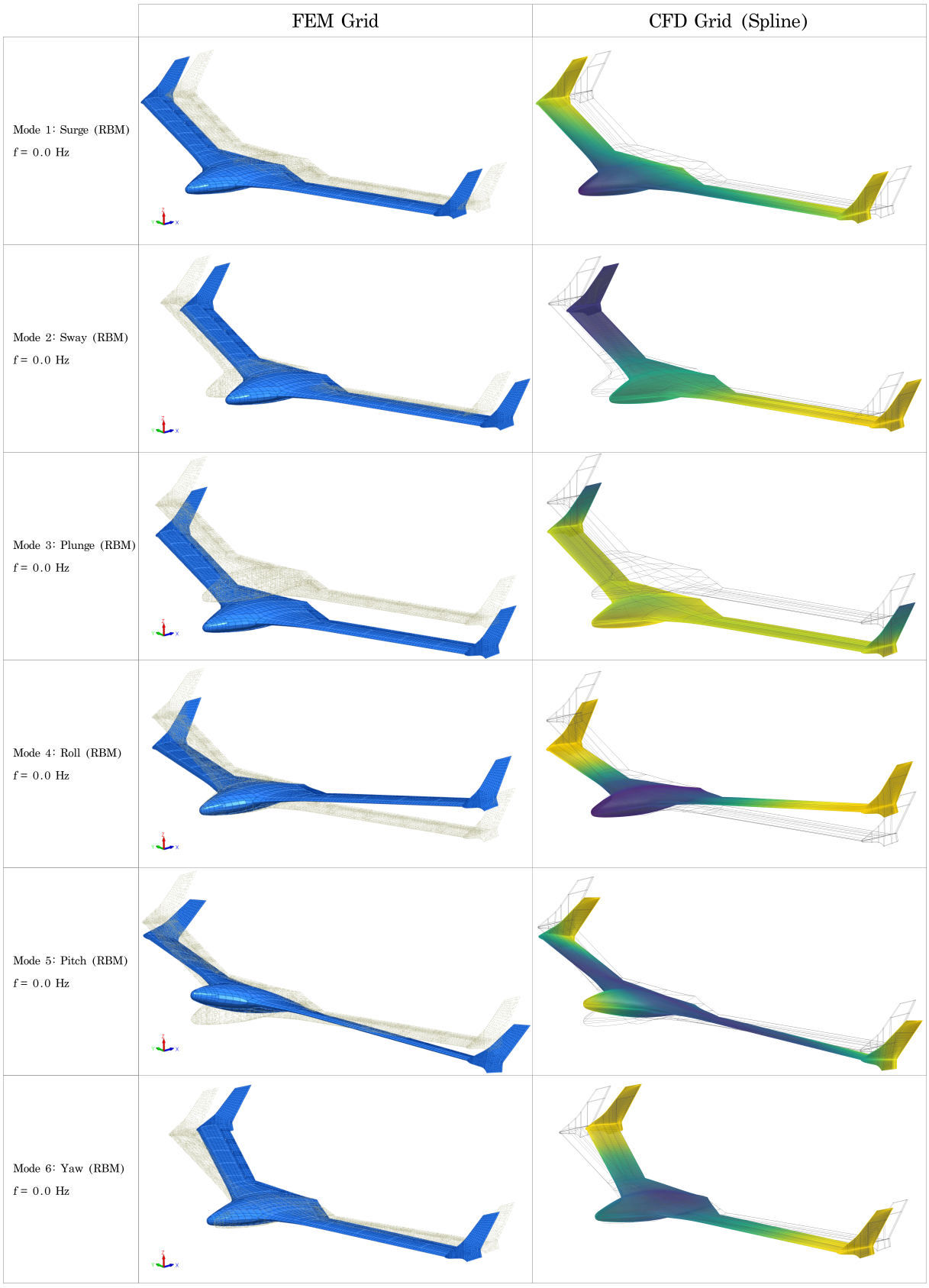

Figure 15: Rigid Body Modes on FEM and CFD grids

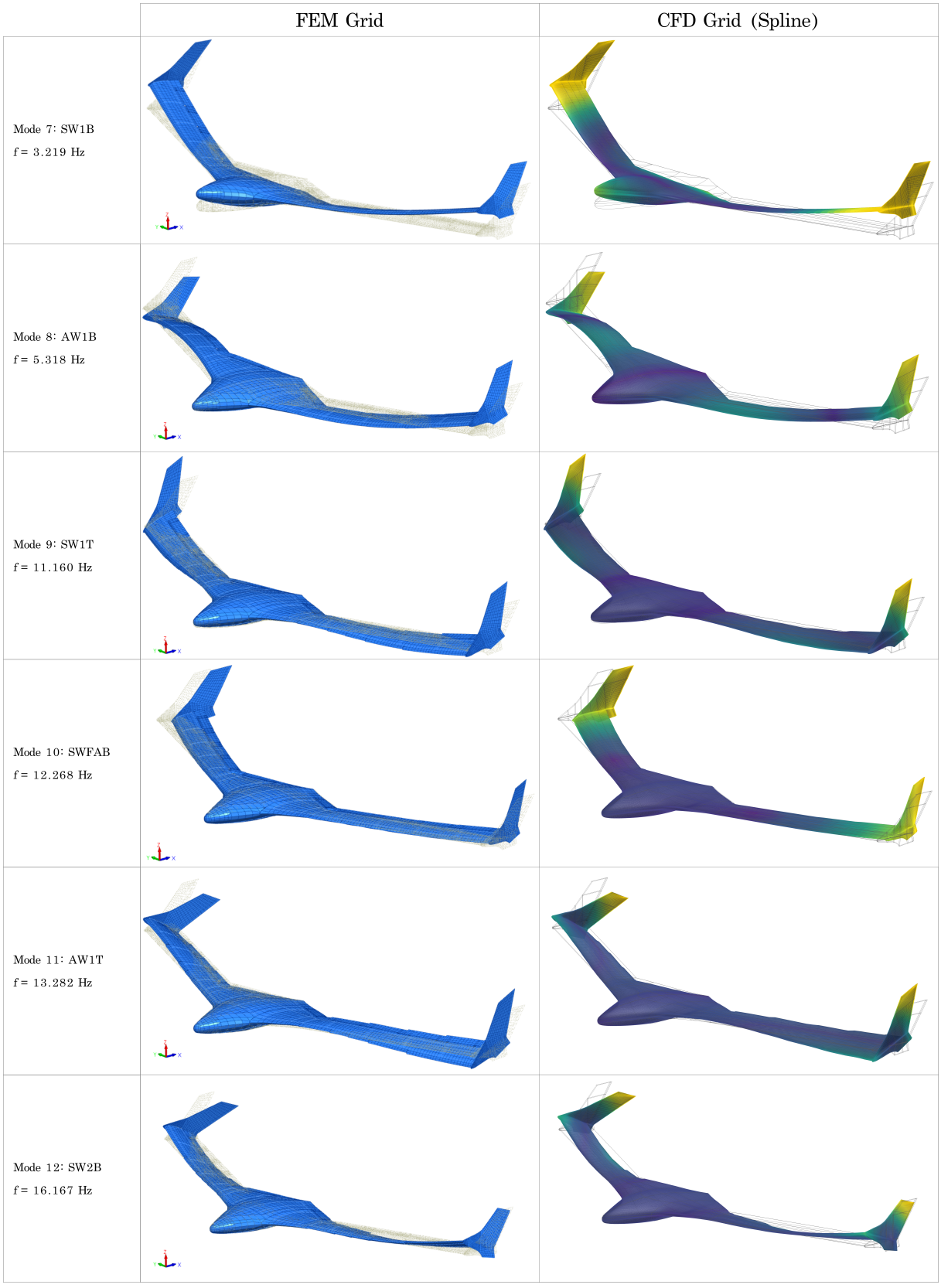

Figure 16: Flexible Modes on FEM and CFD grids.

4.4 Generation of Generalised Aerodynamic Forces

The Generalised Aerodynamic Forces were computed through *forced vibrations* simulations using the ENSOLV unsteady RANS flow model. The computations were performed on the X-56 jig shape, using the corresponding steady RANS solution as the initial flow condition for the subsequent unsteady analyses.

The total number of computations required to collect the complete GAF data set amounted to the product of the number of analysed modes and the number of considered reduced frequencies. Each mode was analysed for 21 reduced frequencies ranging $0 < K_{EN} < 1$.The analyses were repeated 15 times, exciting each mode consecutively. Hence the complete analysis entailed 15 modes times 21 reference reduced frequencies, resulting in a total of 315 simulations.

The excitation signal used for the grid deformation was a sine function of amplitude 0.05 and frequency $k_{EN_i}\,(i = 1, 2, ...N_k; N_k = 21; k_{EN_1} \approx 0; k_{EN_{21}} = 1.9969)$, simulated over 3 periods. Note that k_{EN} is the reference reduced frequency as defined in ENSOLV w.r.t. to the characteristic length $L_{ref} \equiv c$. This means that that the reduced frequency k as defined in the literature (Eq. 22) and used in ZAERO analyses, is half the value of those used in ENSOLV $(k = 1/2k_{EN})$. More on the multi-block grid deformation feature in ENSOLV and its CAE functionalities can be found in [18] and [20].

After performing a series of time-convergence investigations, the number of time steps per period (N_{tpp}) was chosen as 32, totalling 96 time steps for the complete 3-period long simulation run. The time step size was determined by the given k_{EN} value used in the simulation run and the number of time steps per period, N_{tpp}:

$$dT = 2\pi/k_{EN}N_{tpp} \tag{23}$$

For each time step, the flow equations were solved 30 times to reach convergence around the steady flow solution. The significant reduction from 60 to 30 iterations compared to the previous analyses in [8], testifies to the effectiveness of the grid improvement efforts carries out for the present work.

The *high-fidelity* GAFs as defined in Eqs. 17-18 computed in ENSOLV through a series of unsteady RANS analyses (step C. in Fig. 8). The *low-fidelity* GAFs as defined in Eq. 21 were obtained through the ZONA6-based aeroelastic simulations in ZAERO. For the unsteady RANS computations (step C. in Fig. 8), for any given mode, the procedure was to first compute the GAFs for the case $k_{EN_1} \approx 0$, before proceeding with the runs corresponding to k_{EN_i} for $i = 2, ..., 21$. As $k_{EN_1} \approx 0$ approximates the steady state solution, comparing this unsteady solution to the steady flow computations of the undeformed shape (step B. in Fig. 8) served as a verification step. The unsteady RANS-based forced vibrations simulations produce time-domain GAFs. The final step is a postprocessing step which transforms the time-domain GAFs to frequency domain through Discrete Fourier Transformation (DFT). The complex valued frequency domain GAFs were collected into a matrix for each reduced frequency, and scaled by the characteristic length (i.e. the chord length) to achieve the same unit normalisation as the results obtained from ZAERO analyses. The resulting ENSOLV GAF matrices are then compared to the ZAERO results.

A selection of the results of this analysis is presented in Figs. 17, 18, and 19, representing results form ENSOLV and ZAERO analyses. All diagonal GAF terms Q_{ii} are shown in Figs.

17 and 18 for RBM and FlexM modes, respectively. The diagonal Q_{ii} are presented in terms of their real and imaginary parts.

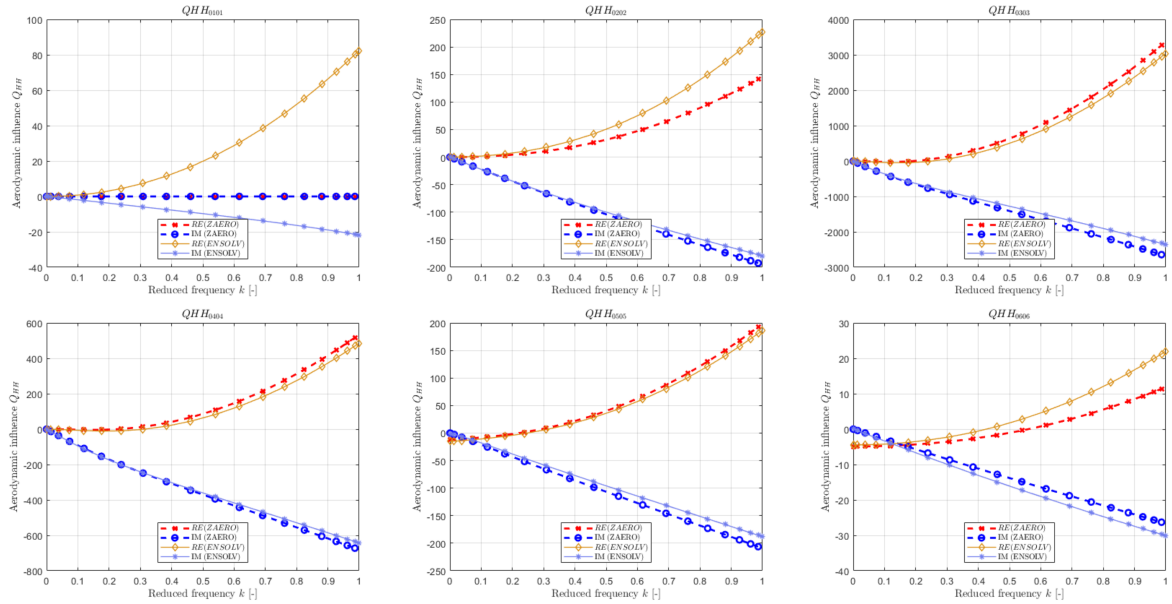

Figure 17: ENSOLV vs. ZAERO: diagonal Generalised Aerodynamic Force (GAF) terms for RBM.

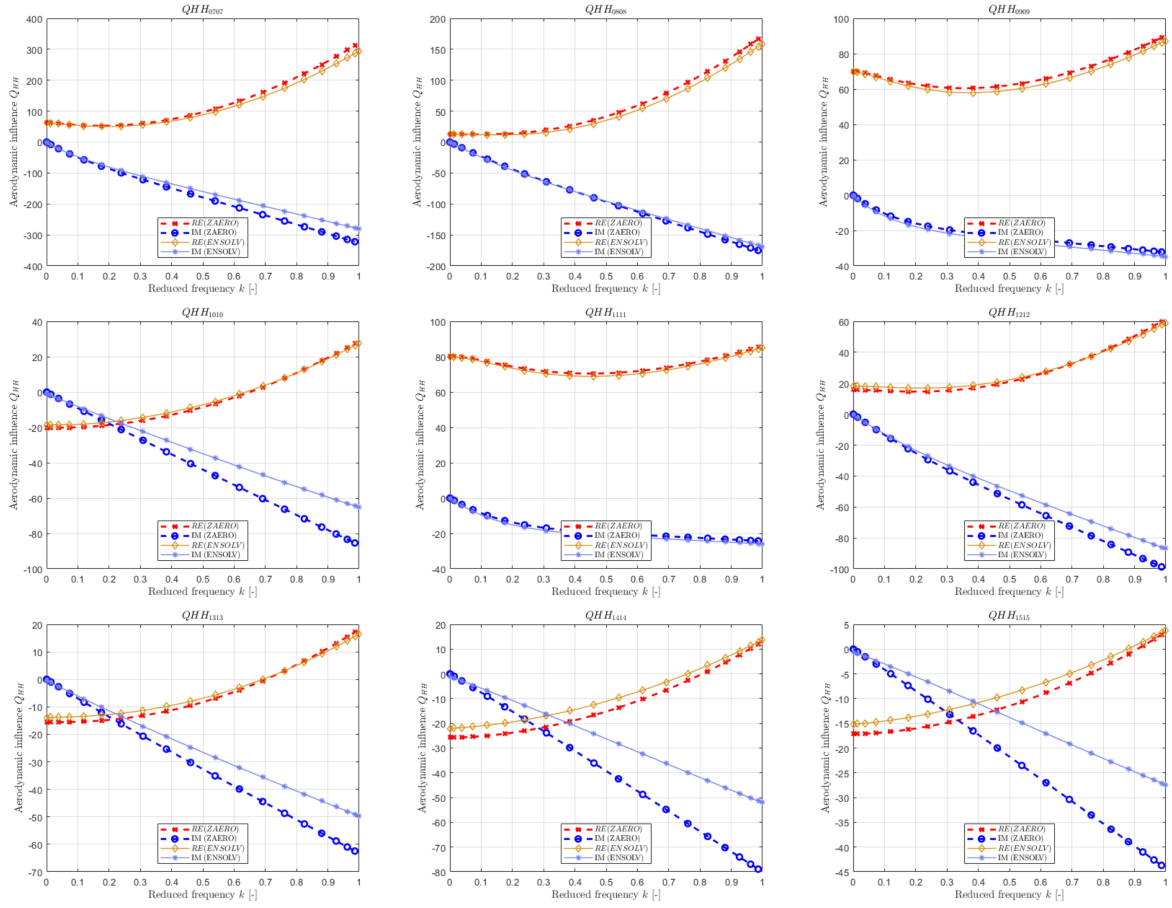

Figure 18: ENSOLV vs. ZAERO: diagonal Generalised Aerodynamic Force (GAF) terms for FlexM.

In addition, a selection of off-diagonal GAFs Q_{ij} is presented in Fig. 19; these terms relay the effects of certain modes on one another. Namely, $Q_{5,7}$ and $Q_{7,5}$ represent the effect on SW1B (M7) due to Pitch (M5), vice versa, which represents the coupling mechanism behind the BBF flutter mode. Similarly, $Q_{7,9}$ and $Q_{9,7}$ represent the interaction between the SW1B (M7) and SW1T (M9) modes, which is the governing mechanism behind the SWBT flutter mode. Finally, $Q_{8,11}$ and $Q_{11,8}$ represent the interaction between the AW1B (M8) and AW1T (M11) modes which defines the mechanism behind the AWBT flutter mode.

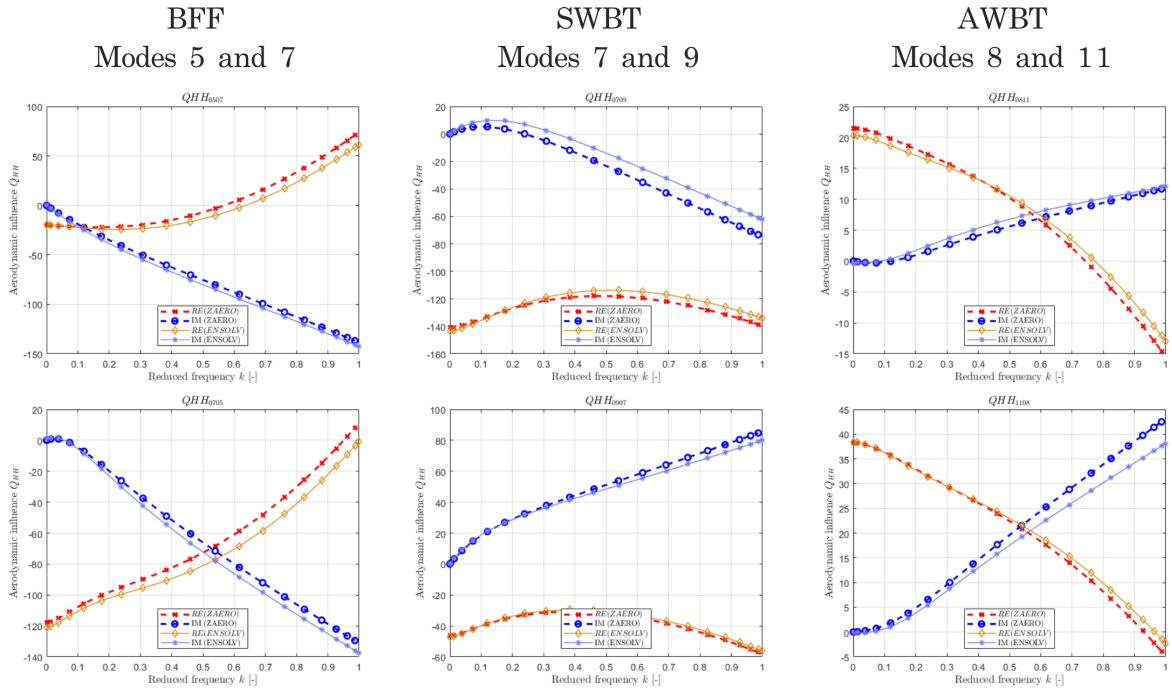

Figure 19: ENSOLV vs. ZAERO: off-diagonal Generalised Aerodynamic Force (GAF) terms for 3 Flutter modes.

The ENSOLV and ZAERO results are a close match for lower reduced frequencies where the flow can be assumed to be (quasi)-steady. With increasing k_{EN_i}, corresponding to increasing flow unsteadiness, divergence between the results of the low- and high- fidelity simulations was expected. The trends, however. are similar. The only major difference is in the first RBM (Surge), a motion that cannot be computed using a panel method. The results presented in this section show a significant improvement compared to the results from prior work [8], attesting to the effectiveness of the analysis improvement measures implemented for the recent study.

4.5 Flutter analyses

X-56A was developed to exhibit three flutter phenomena within its flight envelope characterised by the coupling of (low frequency) flexible structural modes with the aircraft's rigid body motion. The first dynamic instability exhibited by this model is the Body Freedom Flutter (BFF) phenomenon which onsets due to the coupling between the rigid body short period flight dynamic mode and the first flexible wing bending mode. The other to instabilities are the symmetric wing bending-torsion (SWBT) flutter, and the anti-symmetric wing bending-torsion (AWBT) flutter. The flutter analyses presented here (Fig. 20 were obtained based on ZAERO GAF calculations. This analysis used a different set of rigid body modes (RBM). The first two RBM modes in this set exhibited a coupled pitch motion as opposed to the pure pitch mode (mode 5) in the new analysis set. In Fig. 20, the instability of mode 7 corresponds to BFF flutter mode;

mode 9 corresponds to SWBT flutter mode. The AWBT (not displayed as flutter mode in the figures), corresponds to mode 11. Figure 20 shows the 10lb fuel state results.

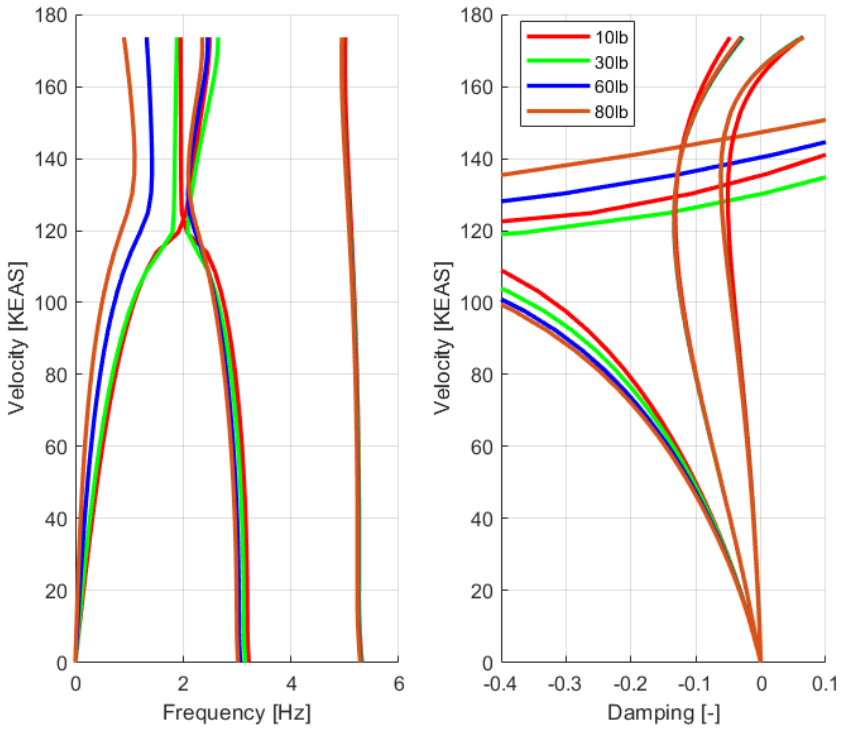

Figure 21: Flutter diagram for the different fuel cases. Results obtained from ZAERO.

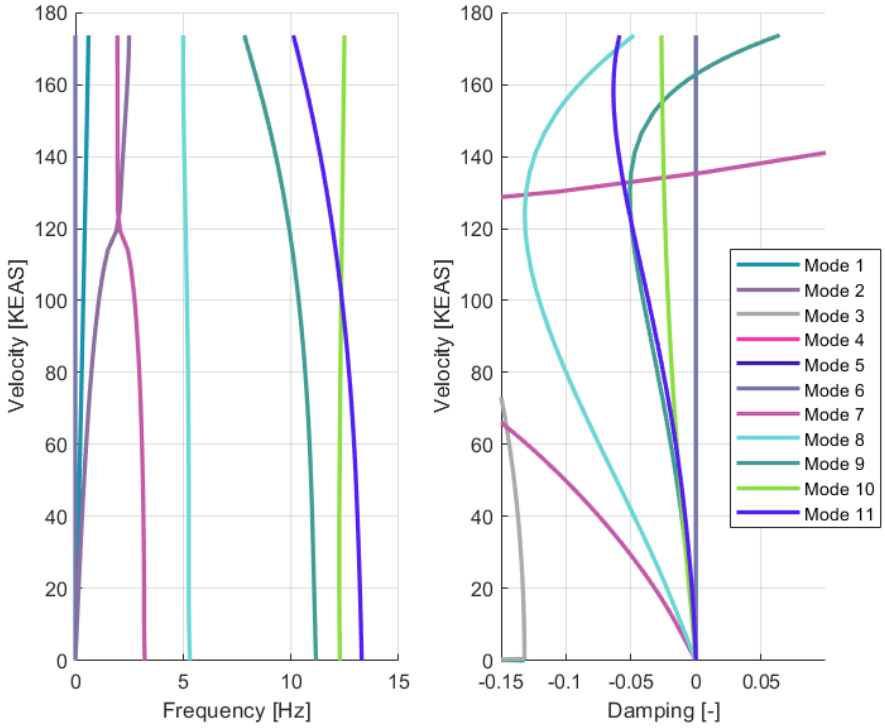

Figure 20: Flutter diagram for the 10lb fuel case. Results obtained from ZAERO.

Figure 21 compares the effects of the different fuel states (10lb, 30lb, 60lb and 80lb).

The natural frequencies at zero velocity are consistent with NASTRAN results, summarised in Table 6 and show decrease with increasing mass. This results in a slightly higher flutter velocity for the 80lb mass case compared to the lower fuel states (10lb and 30lb).

		Natural Frequencies, f [Hz]			
Mode	Description	10 lb	30 lb	60 lb	80 lb
7	SW1B	3.22	3.15	3.06	3.02
8	AW1B	5.32	5.31	5.30	5.29
9	SW1T	11.16	11.15	11.13	11.12
10	SWFAB	12.27	12.23	12.18	12.15
11	AW1T	13.28	13.27	13.26	13.25

Table 6: Natural frequencies for different modes and fuel cases.

5 CONCLUSIONS

The current status of the work from the Netherlands Aerospace Centre (NLR) within the Third Aeroelastic Prediction Workshop (AePW-3) Flight Test Working Group has been presented. Two different unsteady aerodynamic models were implemented to investigate the dynamic instabilities exhibited by the X-56A Multi-Utility Technology Testbed (MUTT): a lower fidelity panel method, ZONA6, developed by ZONA Technology for ZAERO, and a high-fidelity unsteady RANS-based Computational Fluid Dynamics (CFD) and Computational AeroElastic (CAE) simulations performed using the Navier-Stokes flow solver ENSOLV developed by NLR. The aerodynamic grids of both models were splined for each structural mode shape obtained from the finite element structural dynamic analysis performed in NASTRAN. The X-56A configuration used for this study is the 10lb fuel state model released within the AePW-3 group. To obtain the Generalised Aerodynamic Forces (GAFs) from the unsteady RANS simulations in ENSOLV, a sequence of forced harmonic vibration simulations was performed for each structural mode and for a set of reduced frequencies at one flight condition. The resulting integrated GAFs were compared to the ZAERO results, showing good agreement for both the rigid body and elastic modes. The final flutter analyses, performed in ZAERO, conveyed the expected flutter phenomena.

Building on earlier work, static aeroelastic analyses were performed to determine the flight shape and investigate the effect of wing tip deflection and twist on the steady RANS simulation, in relation to the analysis performed on the jig shape. Earlier studies identified the need for further refinement of the high-fidelity aeroelastic methodology to improve aeroelastic predictions. Efforts presented in this paper included adjustments to methods used in NASTRAN modal analysis in order to achieve pure translational and rotational rigid body modes; significant improvements to the CFD surface and volume grid, resulting in an optimal multi-grid with extended far-field boundaries, improving computational efficiency, convergence and accuracy; refinement of the CFD/CAE procedures and parameters for unsteady computations to achieve improved convergence and accuracy, particularly for unsteady analyses at low-Mach conditions. This research is ongoing, with the next steps potentially involving further investigations into the fuel state effects, exploration of amplitude dependent nonlinearities in the unsteady simulation process, determination of flutter modes using the URANS-generated GAFs, and implementation of strategies to increase the efficiency of the presented procedures.

6 REFERENCES

[1] Massey, S. J., Stanford, B., and Jacobson, K. (2022). Progress on Flutter Analysis of the X-56A for the Third Aeroelastic Prediction Workshop. In *AIAA SCITECH 2022 Forum*. San Diego, CA & Virtual: American Institute of Aeronautics and Astronautics. ISBN 978-1-62410-631-6. doi:10.2514/6.2022-2315.

[2] Lockheed Martin Corporation (2023). X-56a multi-utility technology testbed (mutt). `https://www.lockheedmartin.com/en-us/products/X-56A.html`. Accessed: 2023-06-16.

[3] Ryan, J. J. and Bosworth, J. T. (2014). Current and Future Research in Active Control of Lightweight, Flexible Structures Using the X-56 Aircraft. In *52nd Aerospace Sciences Meeting*. National Harbor, Maryland: American Institute of Aeronautics and Astronautics. ISBN 978-1-62410-256-1. doi:10.2514/6.2014-0597.

[4] Ouellette, J. A., Massey, S., Grauer, J. A., et al. (2024). Summary of Results from the Third Aeroelastic Prediction Workshop Flight Test Working Group. In *AIAA SCITECH 2024 Forum*. Orlando, FL: American Institute of Aeronautics and Astronautics. ISBN 978-1-62410-711-5. doi:10.2514/6.2024-0415.

[5] NASA Armstrong Flight Research Center (2021). Nasafacts: X-56a multi-utility technology testbed (mutt). Online. Accessed: 2024-06-16.

[6] Grauer, J. and Boucher, M. (2019). Identification of Aeroelastic Models for the X-56A Longitudinal Dynamics Using Multisine Inputs and Output Error in the Frequency Domain. *Aerospace*, 6(2), 24. ISSN 2226-4310. doi:10.3390/aerospace6020024.

[7] Reasor, D. A., Bhamidipati, K. K., and Chin, A. W. (2016). X-56A Aeroelastic Flight Test Predictions. In *54th AIAA Aerospace Sciences Meeting*. San Diego, California, USA: American Institute of Aeronautics and Astronautics. ISBN 978-1-62410-393-3. doi:10.2514/6.2016-1053.

[8] Timmermans, H. S., Aalbers, V. J. E., and Mkhoyan, I. A. (2022). Flutter Analyses of the X-56 Unmanned Aerial Vehicle within the AePW-3 Flight Test Working Group. In *Proceedings of the International Forum on Aeroelasticity and Structural Dynamics (IFASD)*. Madrid, Spain: International Forum on Aeroelasticity and Structural Dynamics.

[9] Beranek, J., Nicolai, L., Buonanno, M., et al. (2010). Conceptual Design of a Multi-Utility Aeroelastic Demonstrator. In *13th AIAA/ISSMO Multidisciplinary Analysis Optimization Conference*. Fort Worth, Texas: American Institute of Aeronautics and Astronautics. ISBN 978-1-60086-954-9. doi:10.2514/6.2010-9350.

[10] Nicolai, L., Hunten, K., Zink, P. S., et al. (2010). System Benefits of Active Flutter Suppression for a SensorCraft-Type Vehicle. In *13th AIAA/ISSMO Multidisciplinary Analysis Optimization Conference*. Fort Worth, Texas: American Institute of Aeronautics and Astronautics. ISBN 978-1-60086-954-9. doi:10.2514/6.2010-9349.

[11] Bismarck-Nasr, M. N. (1999). *Structural dynamics in aeronautical engineering*. Reston, VA: American Institute of Aeronautics and Astronautics. ISBN 978-1-56347-323-4 978-1-60086-245-8. OCLC: 849923029.

[12] Hodges, D. H. and Pierce, G. A. (2011). *Introduction to Structural Dynamics and Aeroelasticity*. Cambridge University Press, 2 ed. ISBN 978-0-521-19590-4 978-0-511-99711-2 978-1-107-61709-4. doi:10.1017/CBO9780511997112.

[13] Brincker, R. and Ventura, C. (2015). *Introduction to operational modal analysis*. Chichester, West Sussex: John Wiley and Sons, Inc. ISBN 978-1-118-53515-8 978-1-118-53516-5.

[14] (2016). ZAERO Theoretical Manual v.9.2. Tech. rep., ZONA Technology, Inc, Scottsdale, AZ.

[15] Chen, P. C. and Bhasin, S. (2012). ZONA6 Versus the Doublet-Lattice Method for Unsteady Aerodynamics on Lifting Surfaces. *Journal of Aircraft*, 49(3), 966–968. ISSN 0021-8669, 1533-3868. doi:10.2514/1.C031648.

[16] (2020). ZAERO User's Manual v.9.3. Tech. rep., ZONA Technology, Inc, Scottsdale, AZ.

[17] Kok, J., Boerstoel, J., Kassies, A., et al. A robust multi-block Navier-Stokes flow solver for industrial applications. Technical Report NLR TP 96323, The Netherlands.

[18] Spekreijse, S., Prananta, B., and Kok, J. (2002). A simple, robust and fast algorithm to compute deformations of multi-block structured grids. Technical Report NLR-TP-2002-105, Netherlands Aerospace Center.

[19] Kok, J. C. and Spekreijse, S. P. (2000). Efficient and accurate implementation of the k–ω turbulence model in the NLR multi-block Navier–Stokes system. In *ECCOMAS 2000*. Barcelona, Spain. NLR-TP-2000-144.

[20] Prananta, B., Kok, J., Spekreijse, S., et al. (2003). Simulation of limit limit cycle oscillation of fighter aircraft at moderate angle of attack. In *International Forum on Aeroelasticity and Structural Dynamics*. Amsterdam, the Netherlands. NLR-TP-2003-526.

[21] MSC Software Corporation (2021). *MSC Nastran 2021 Dynamic Analysis User's Guide*. Available from MSC Software Corporation.

[22] Kok, J. C. (2000). Resolving the dependence on freestream values for the k–ω turbulence model. *AIAA Journal*, 38(7), 1292–1294.

[23] Dol, H., Kok, J., and Oskam, B. (2002). Turbulence modelling for leading-edge vortex flows. In *40th AIAA Aerospace Sciences Meeting & Exhibit*. Reno,NV,U.S.A.: American Institute of Aeronautics and Astronautics. doi:10.2514/6.2002-843.

COPYRIGHT STATEMENT